Evaluation of Contemporary Ocean Wave Models in Rare Extreme Events: The "Halloween Storm" of October 1991 and the "Storm of the Century" of March 1993

V. J. CARDONE

Oceanweather Inc., Cos Cob, Connecticut

R. E. JENSEN

Coastal Engineering Research Center, USAE Waterways Experiment Station, Vicksburg, Mississippi

D. T. RESIO

Florida Institute of Technology, Melbourne, Florida

V. R. SWAIL

Environment Canada, Downsview, Ontario, Canada

A. T. COX

Oceanweather Inc., Cos Cob, Connecticut

(Manuscript received 24 October 1994, in final form 10 July 1995)

ABSTRACT

Two recent severe extratropical storms, the "Halloween storm" of October 26–November 2 1991 (HOS) and the "storm of the century" (SOC) of March 12–15 1993, are characterized by measurements of sea states of unprecedented magnitude off the east coast of North America. A Canadian buoy moored in deep water south of Nova Scotia recorded peak significant wave heights (HS) exceeding 16 m in both storms. In SOC, a NOAA buoy moored southeast of Cape Hatteras recorded a peak HS of 15.7 m, a record high for NOAA buoys. These extreme storm seas (ESS) exceed existing estimates of the 100-yr estimated design wave in these regions by about 50%. The extensive wave measurements made in both storms from buoys moored in deep water provide a rare opportunity to validate modern ocean wave models in wave regimes far more severe than those used for model tuning. In this study, four widely applied spectral wave models (OWI1G, Resio2G, WAM4, and OWI3G) are adapted to the western North Atlantic basin on fine mesh grids and are driven by common wind fields developed for each storm using careful manual kinematic reanalysis. The alternative wave hindcasts are evaluated against time series of measured HS and dominant wave period obtained at nine U.S. and Canadian buoys moored in deep water between offshore Georgia and Newfoundland. In general, it was found that despite the large differences in model formulation, the hindcasts were almost uniformly skillful in specification of the evolution of wave height and period in these two storms. The skill was much greater than achieved routinely in real time wave analyses provided by some of these same models operating at U.S., Canadian, and European centers, confirming that at least for these particular models, typically large errors in operational surface marine wind field analyses are the dominant source of errors in operational wave analyses and forecasts. However, all models were found to systematically underpredict the magnitude of the peak sea states in both storms at buoys that recorded peak HS in excess of about 12 m (ESS). This bias in ESS wave heights was 3.2 m for OWI1G, 1.9 m for Resio2G, 2.2 m for OWI3G, and 1.5 m for WAM4. These results provide an interesting assessment of the progress made in the past decade in ocean wave modeling, both in terms of improvements of 1G and 2G models, and the introduction of 3G models. The 2G and 3G models show a slight advantage over the 1G model in simulating the most extreme wave regimes. These results suggest strongly that, for applications where supercomputers are not available, and especially for most operational applications where only integrated properties of the spectrum (e.g., HS) are required or where errors in forcing wind fields are typical of real time objective analyses and forecasts, highly developed and validated 1G and 2G wave models may continue to be used. However, accurate specification of ESS is especially critical for application of wave models to determine the extreme wave climate for ship, offshore, and coastal structure design. Therefore, further study is required to isolate the contribution of remaining wind field errors and model physics and numerics to the underprediction of ESS in extreme storms. The common phenomenological link between these two storms in the regions of ESS appears to be wave generation along a dynamic fetch associated with intense surface wind maxima or jet streaks (JS), which maintain high spatial coherency over at least 24 h and propagate at speeds of 15–20 m s^{-1}. ESS were observed only at those buoys directly in the path of the core of such features. This finding suggests that high-resolution wave models are required to model ESS, but these are justified only if the small-scale JS phenomena can be resolved in operational analysis and forecast systems.

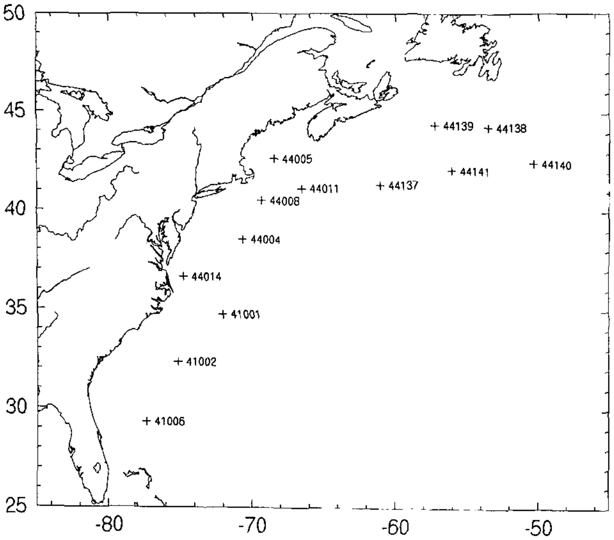

FIG. 1. Locations of U.S. and Canadian data buoys moored in deep water used for hindcast evaluation.

1. Introduction

Numerical ocean wave models have advanced significantly within the past decade, particularly with the introduction of the so-called third-generation (3G) class of models. First- (1G) and second-generation (2G) models have also been improved and remain in widespread use for climate assessment, engineering studies, and operational forecasting. These three wave model classes are differentiated mainly by the simulation of the physics of deep water wave growth and decay. Due to remaining uncertainties in the underlying physics, however, all models rely to some degree on empirical tuning, based mainly on observations of wave growth in stationary fetch-limited wind fields of moderate strength. Such models are then often applied to determine the extreme wave climate in harsh basins for design purposes and to provide guidance in real time to shipping for optimum ship routing and heavy weather damage avoidance. An extensive suite of wave measurements made in two very extreme western North Atlantic storms from buoys moored in deep water provides a rare opportunity to validate these models in wave regimes far removed from those used for model tuning, but comparable to those encountered in the model applications cited above.

In this study, four widely applied spectral wave models, namely Oceanweather's 1G (Cardone et al. 1976) and 3G (Khandekar et al. 1994) models, a 2G wave model (Resio and Perrie 1989), and the 3G WAM4 (WAMDI 1988; Gunther et al. 1991) are adapted to the western North Atlantic basin on grid systems with common resolution and are driven by a common wind field derived for each storm. The wind field was developed using a subjective–objective man–machine mix approach, which used all conventional data, including ship and buoy observations received too late for use in real time. The alternative wave hindcasts were evaluated against time series of measured significant wave height (HS), dominant wave period (TP), and one-dimensional (frequency) wave spectra obtained at nine U.S. and Canadian buoys moored in deep water between offshore Georgia and Newfoundland.

Wave models have been compared in previous studies. For example, the behavior of about a dozen 1G and 2G spectral wave models were evaluated in several standard test cases and intercompared over a decade ago in the SWAMP (1985) exercise. Large differences in behavior were found even for the simplest constant wind fetch- and duration-limited growth tests, suggesting large differences in behavior as well in real applications. In a more recent intercomparison study, nine North Atlantic wave models (one 1G, seven 2G, and one 3G type) were applied to hindcast an 11-day period of the Labrador Sea Extreme Waves Experiment (LEWEX) using both model-specific wind fields and a common wind field, with hindcasts evaluated against in situ and airborne remotely sensed directional wave spectra. The sea state regime of LEWEX was swell dominated and the skill of all hindcasts appeared to

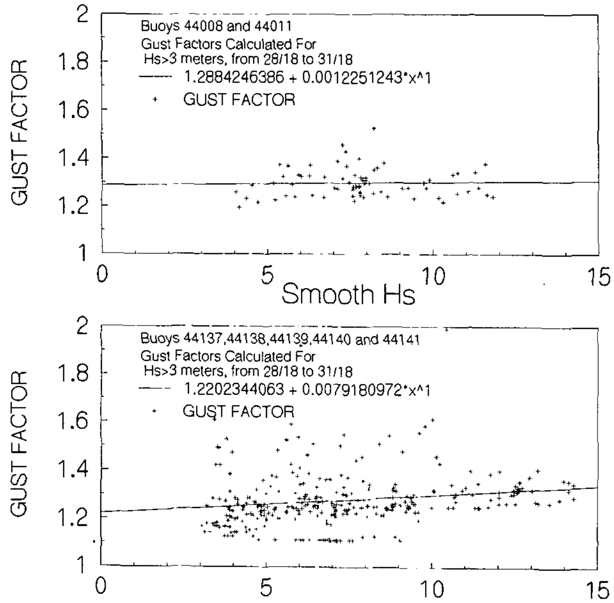

FIG. 2. Gust factor (reported gust wind speed/reported average wind speed) vs significant wave height (3-h average, heights) in Halloween storm for buoys (above) reporting scalar wind speed averages and buoys (below) reporting vector wind speed averages.

Corresponding author address: Dr. V. R. Swail, Climate and Atmospheric Research Directorate, Environment Canada, 4905 Dufferin Street, Downsview, ON M3H 5T4 Canada.
E-mail: Vswail@dow.on.doe.ca

TABLE 1. List of meteorological and oceanographic buoys.

Station	Selected for	Water depth	Latitude	Longitude	Anem. height	Pay load	Hull	Location
44142		1500	42°29.6′N	64°12.0′W	5.4 m	C	C6N07	La Have Bank
44141	HOS, SOC	4500	42°04.0′N	56°09.1′W	5.4 m	C	C6N12	Laurentian Fan
44140	HOS	1400	42°43.8′N	50°36.4′W	5.4 m	C	C6N09	Tail of the Bank
44139	HOS, SOC	1100	44°19.2′N	57°21.2′W	5.4 m	C	C6N06	Banquereau
44138	HOS, SOC	1500	44°13.8′N	53°38.0′W	5.4 m	C	C6N10	SW Grand Banks
44137	HOS, SOC	4500	41°11.6′N	61°07.8′W	5.4 m	C	C6N11	East Scotian Slope
44025		40	40°15.0′N	73°10.0′W	5.0 m	D	3D21	Long Island
44014	SOC	48	36°35.0′N	74°50.0′W	3.5 m	D	3D31/3D20	Virginia Beach
44013		30	42°22.6′N	70°46.6′W	13.8 m	D	LNB11	Boston Harbor
44012		24	38°47.6′N	74°34.6′W	13.8 m	D	LNB01	Five Fathoms
44011	HOS	88	41°04.9′N	66°34.6′W	5.0 m	D	6N16	Georges Bank
44009		28	38°27.0′N	74°42.0′W	13.8 m	D	LNB06	Delaware Bay
44008	HOS	60	40°30.0′N	69°25.7′W	13.8 m	D	LNB07/02	Nantucket
44007		47	43°31.6′N	70°05.4′W	13.8 m	D	LNB09	Portland
44005	SOC	202	42°37.9′N	68°33.1′W	5.0 m	D	6N02	Gulf of Maine
44004	SOC	3231	38°32.2′N	70°42.3′W	5.0 m	D	6N19/6N29	"Hotel"
41016		1586	24°38.2′N	76°31.3′W	10.0 m	G	12D9	Eleuthera
41010		833	28°52.8′N	78°32.0′W	10/5 m	D	10D8/6N28	E. Cape Canaveral
41009		41	28°30.0′N	80°10.8′W	5.0 m	D	3D17/10D11	Cape Canaveral
41008		18	30°43.6′N	81°04.8′W	5.0 m	D	3D16	E. Jacksonville
41006	SOC	1042	29°18.7°N	77°22.9′W	5.0 m	D	6N06	E. Daytona
41004			32.5°N	79.1°W	5.0 m	D	3D29	Edisto
41002	HOS, SOC	3658	32°17.7′N	75°14.4′W	5.0 m	G/D	6N23	S. Cape Hatteras
41001	HOS	4206	34°55.5′N	72°57.1′W	5.0 m	D	6N07	E. Cape Hatteras

Hull: 6N—6 m NOMAD; 3D—3-m discus; LNB—large navigational buoy; 12D—12-m discus; 10D—10-m discus.
Payload: C—Canadian; D—DACT; G—GSBP.

suffer from unavoidably large errors in the wind field in swell source zones, which happened to be located outside the North Atlantic shipping lanes (Beal 1991).

The evaluation of the 1G and 2G models that have been applied operationally for real-time analysis and forecasting over the past decade (e.g., Clancy and Sadler 1992; Guillaume 1990) and in historical hindcasting studies (e.g., Cardone and Ewans 1992) indicate greater and more uniform skill than implied by the SWAMP experience. Typically, in Northern Hemisphere basins, and when driven by conventionally produced wind fields, time series of HS are specified with bias of less than 0.5 m, rms difference ranging between about 0.75 m in summer to 1.25 m in winter, and scatter index (ratio of rms difference to mean of verification data sample) of 25%–50%. Spectral peak period is usually specified with bias of less than 1.0 s and standard deviation of about 1.5 s. Statistics of wave direction skill are still rarely reported.

There is a growing trend toward implementation of the WAM model (WAMDI Group 1988) for global and regional analysis and forecasting [e.g., the global implementation of cycle 4 of WAM is described by Gunther et al. (1991); the North Sea implementation of WAM known as NEDWAM is described by Burgers (1990); and the Mediterranean Sea version of WAM run at the U.S. Navy Fleet Numerical Meteorology and Oceanography Center (FNMOC) is described by Clancy and Sadler (1992)].

WAM4 was also used to hindcast an 11-day stormy period sampled during SWADE (Cardone et al. 1994), driven by six alternative wind fields. One of the wind fields was carefully developed by mainly hand kinematic analysis with the aid of the SWADE meteorological data, the other five were produced by objective analysis with three of those five actually the standard products of operational centers. The winds derived by manual kinematic analysis provided the lowest wave hindcast errors reported thus far. The scatter index varied between about 10% within the SWADE array to about 20% on the open sea boundary of the buoy array. Errors for the objectively analyzed winds were two to four times greater than for the kinematically derived wind fields. This finding is conditioned on the rather modest range of sea states available for model verification in SWADE, where the peak sea state measured was about 8 m. Since WAM4 requires a supercomputer for most practical applications, it would be of interest to quantify the performance of highly developed 1G and 2G models relative to that of 3G models for meteorological forcing covering a wide dynamic range. Such a range is provided by the two well-documented storms studied herein.

Of the many intense extratropical storms generated off the east coast of North America within the last three cold seasons (since 1991/92), two are also characterized by sea states of unprecedented magnitude: the "Halloween storm" of 26 October–2 November 1991

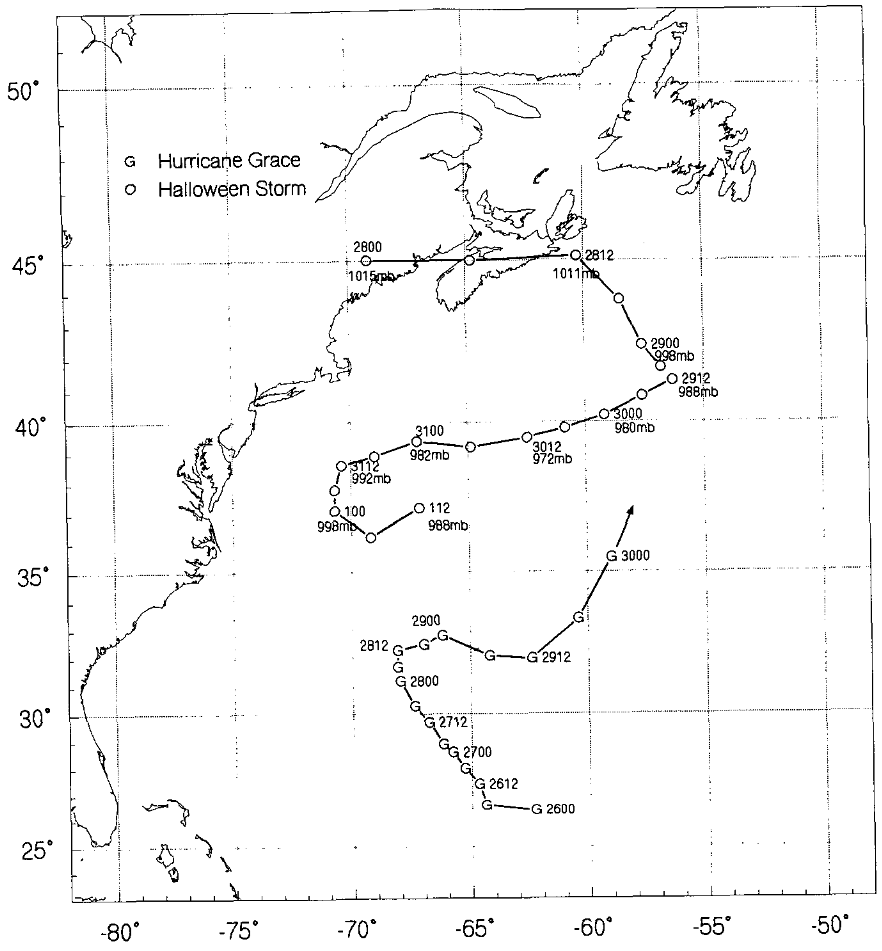

FIG. 3. Track and central pressure of the Halloween storm and southern tropical system.

(HOS) and the "storm of the century" (SOC) of 12–15 March 1993. At Environment Canada buoy 44137, moored in deep water south of Nova Scotia, the measured peak significant wave height (HS) exceeded 16 m in both storms, with maximum crest-trough amplitudes exceeding 30 m (nearly 100 ft). These wave heights exceed current estimates of 100-yr return period wave height extremes in deep water south of Nova Scotia (Eid et al. 1992) by about 50%. At NOAA buoy 41002, moored east of South Carolina, the peak measured HS in the SOC was 15.7 m, an all time record high for NOAA buoys and again exceeding current estimates of design wave heights in that area by a wide margin [e.g., the WIS estimate (Corson et al. 1981) for this site is about 12 m for the 100-yr condition]. We shall refer to *sea states* of such magnitude (say HS greater than 12 m or so) as extreme storm seas (ESS). The immense *single maximum waves* that may occur within such sea states have been dubbed recently extreme storm waves (ESW) (Nickerson 1993) as an alternative to the more popular descriptors "rogue waves" and "freak waves."

This paper is organized as follows. In section 2 we give a concise description of the meteorological and wave data referred to in the study of both storms. Section 3 describes the wind field analysis methodology and the evolution of the major kinematic properties of the generated wind fields. Section 4 gives a brief description of each wave model used and the strategy of the modeling experiments. Section 5 presents the assessment of the accuracy of the alternative wave hindcast models drawn from evaluation of the wave hindcasts analysis against buoy measurements. Finally, in section 6 we discuss the main results and assess their significance.

2. Data sources

A large amount of meteorological and oceanographic data was available for analysis and verification in these two storms, including observations from the Canadian and U.S. buoy networks operating off the east coast of North America, coastal stations, both manned and automatic, and observations

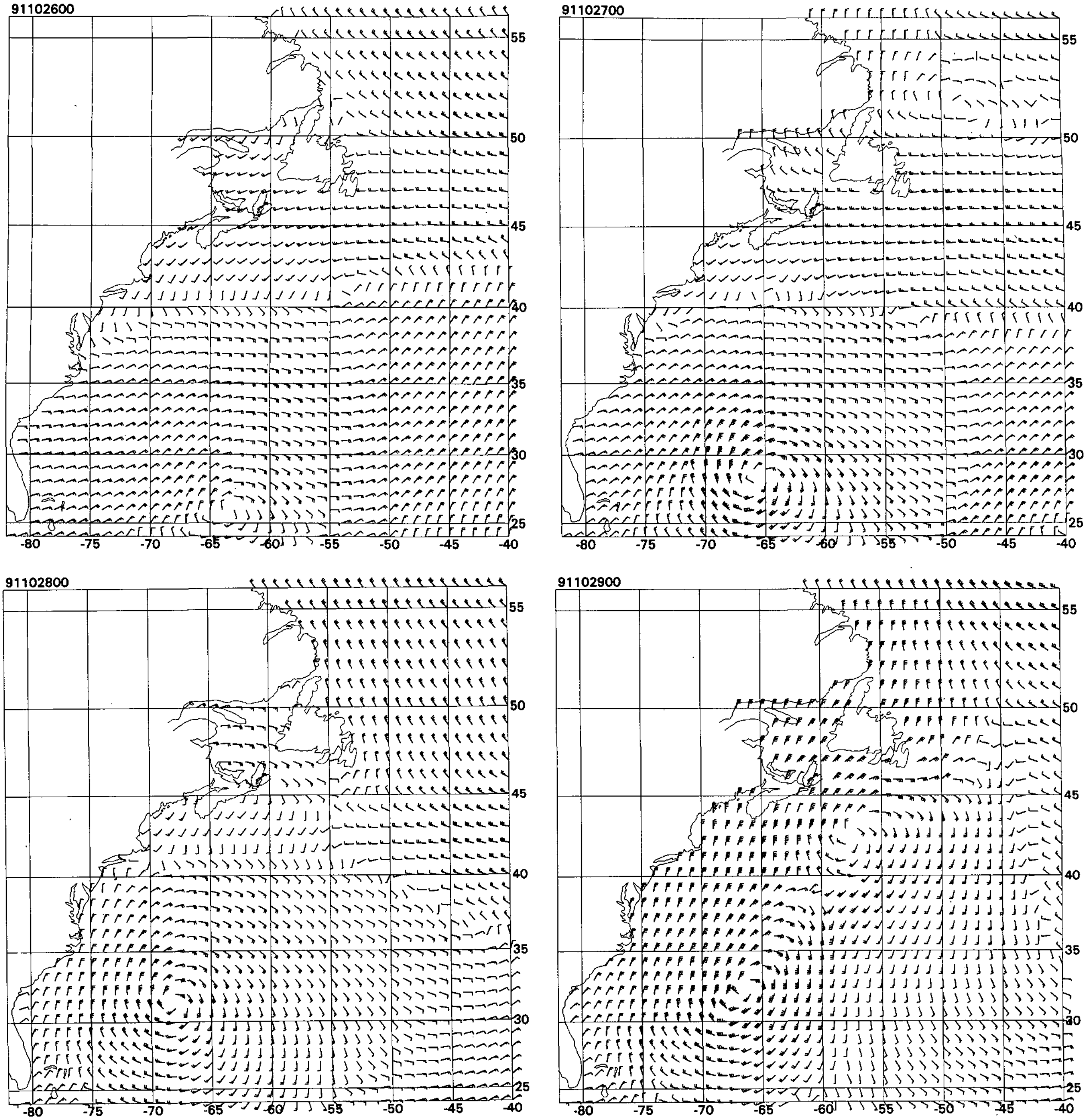

FIG. 4. Reanalyzed surface wind fields in the Halloween storm at 24-h intervals (a)–(g), 0000 UTC 25 October–0000 UTC 1 November 1991. Wind barbs represent effective neutral 1-h average wind speed at 20-m height (kt).

from ships of opportunity in the northwest Atlantic Ocean. The following paragraphs briefly describe the characteristics and interpretation of these data sources.

The most important observations for this study were the measurements of winds and waves made from the Canadian and U.S. meteorological and oceanographic buoys. The buoy wind measurements were the primary input to the kinematic analysis, while the wave measurements provided the verification for the wave model output. Environment Canada operates six 6-m NOMAD buoys, offshore and in deep water; the National Oceanic and Atmospheric Administration (NOAA) maintains a series of buoys, both along the coast in relatively shallow water, and offshore in deep water. The locations of the buoys are shown in Fig. 1; detailed information on the parameters observed by the buoys is given in Table 1.

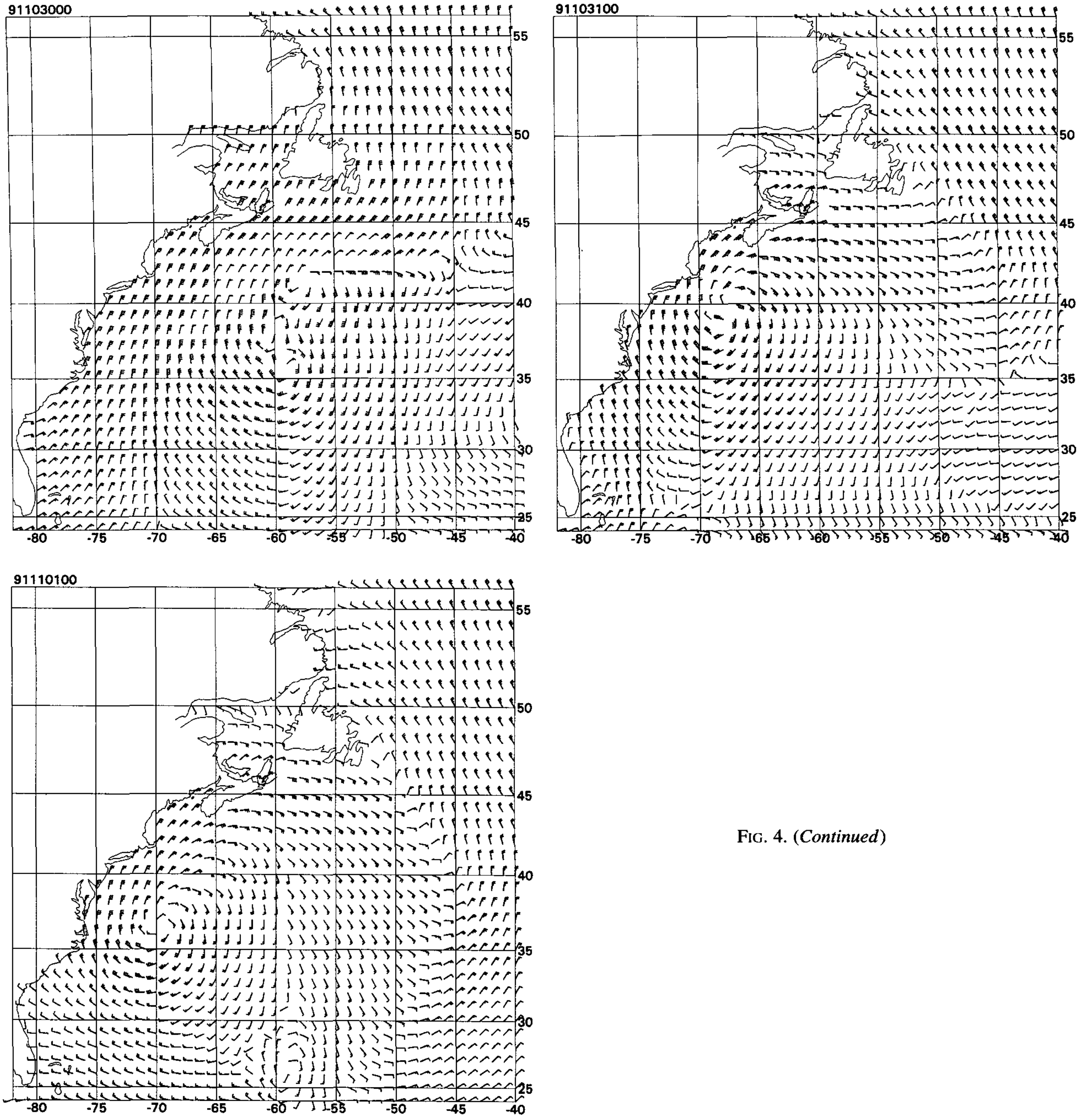

FIG. 4. (*Continued*)

The most important characteristics of the buoy measurements in relation to this study are

(i) winds from the NOAA buoys are 8.5-min *scalar* average speeds, and directions are unit vector averages;

(ii) winds from the Canadian buoys are 10-min *vector* average speeds and directions;

(iii) winds from the NOAA buoys may be at either a 5, 10, or 13.8-m level, and wind observations from the Canadian NOMAD buoys are at 5.4 m;

(iv) Canadian buoys also reported the highest 8-s running scalar mean peak wind speed in the 10-min sample;

(v) Canadian and U.S. nondirectional wave measurements used a "strapped down" accelerometer aligned with the buoy's mast, with the exception of buoy 44139, which employs a gimbaled Datawell heave sensor; the directional buoys (44014, 44025) use a gimbaled Hippy 40 sensor;

(vi) Canadian buoys sample waves at 1 Hz for 35 min; the NOAA buoys sample at 2.56 Hz (DACT) or 1.5 HZ (GSBP) for 20 min; and

(vii) significant wave height in tenths of meters and peak period in tenths of seconds computed from the sample is recorded, along with the 1D (or 2D) spectra.

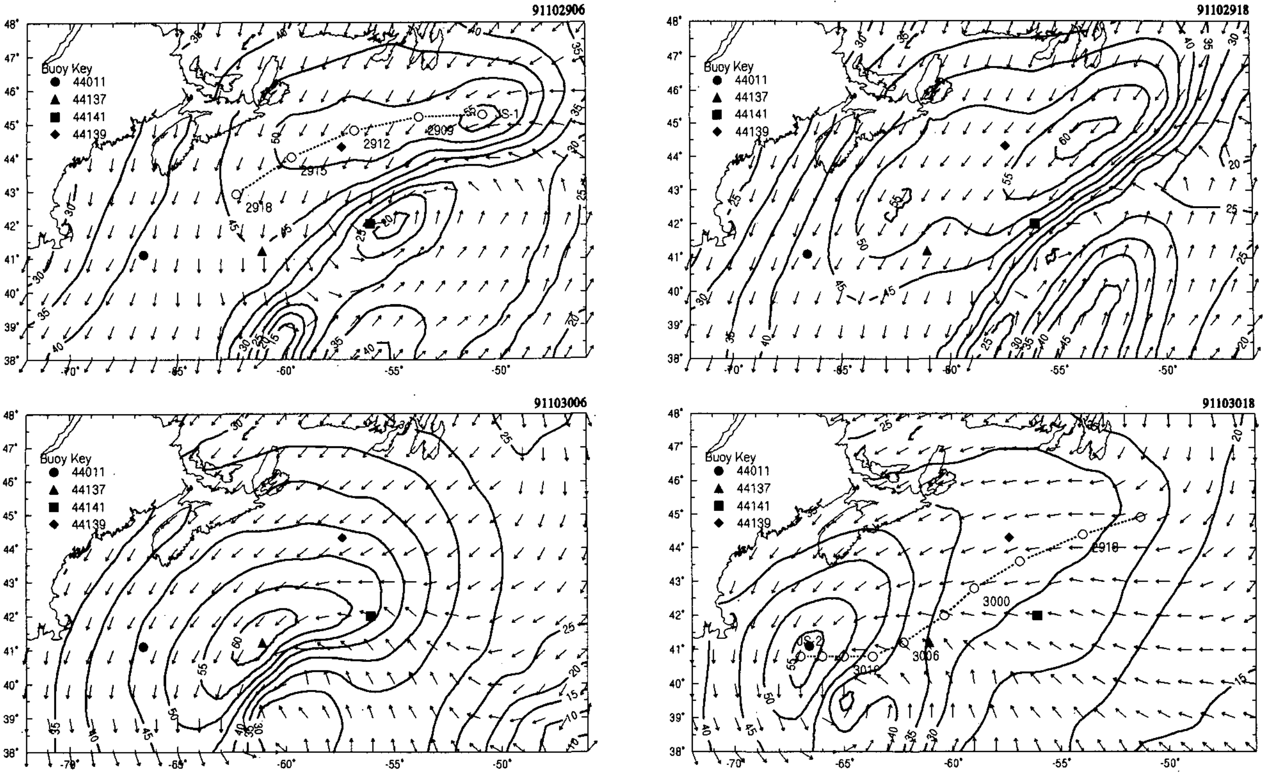

FIG. 5. Twelve-hour (a)–(d) surface wind field analyses in the immediate vicinity of the Halloween storm, showing evolution of major circulation features including jet streaks between 0600 UTC 29 October and 1800 UTC 30 October.

The detailed specifications for the NOAA buoy payloads in operation during these events is given in NCDC (1993a) and Axys Environmental Systems Ltd. (1992). For waves, the total measurement system accuracy is usually quoted as ±0.2 m or 5% for HS and ±1 s for TP. However, a larger uncertainty results from the effect of sampling variability, which for typical buoy sample lengths imparts an uncertainty of 10%–15% in HS and ±5% in TP (Donelan and Pierson 1983).

Winds from ships-of-opportunity were a mixture of anemometer measurements and Beaufort estimates. These were adjusted to provide consistent input to the kinematic analysis as described in section 3. Wave estimates from ships were not used in the study. Winds from manned and automated coastal stations were also used in the kinematic analysis, with subjective corrections to account for land-based effects (e.g., increased surface friction).

3. Wind fields

a. Analysis method

The objective of the wind field analysis is basically to describe the evolution of the surface wind field over a domain of spatial and temporal resolution sufficient to hindcast the maximum sea states experienced off the east coasts of the United States and Canada. After consideration of the extent of the storm circulations and the time of occurrence of the peak waves at the buoys, the following wind field attributes were adopted:

spatial domain 23°–67°N, 30°–82°W
grid system 0.5° × 0.5° latitude–longitude
time step 3-h analyses (interpolated to 1 h)
reference 20-m effective neutral wind speed

storm history
HOS 0000 UTC 25 October–1800 UTC 1 November 1991
SOC 0000 UTC 11 March 1993–0000 UTC 17 March 1993.

In addition to the measured data, the following surface analyses were referred to

NOAA Northern Hemisphere surface analysis—final analysis
NOAA National Hurricane Center (NHC) surface analysis
METOC Halifax surface analysis.

The particular wind analysis approach followed, described by Cardone et al. (1980), attempts to blend the advantages of classical manual analysis with modern objective techniques. The advantages of manual analysis for marine surface weather analyses have been recently emphasized by Sanders (1990) and Uccellini et al. (1992), and there is indeed a trend at NWP centers to maintain and facilitate the use of hand analysis through the use of analyst-friendly graphical interfaces implemented on powerful workstations (e.g., Kocin et al. 1991; Swail 1992). The analysis method consists of the following basic steps.

1) DATA PREPROCESSING

The first step is data preprocessing to identify and filter from the synoptic data stream obviously erroneous data. For buoys, measurements are made by calibrated instruments so errors arise mainly in miscoded or mislocated data and transmission errors, which are easily screened due to the relatively small volume of data involved in this study by visual scans of time series of observations from each platform. The quality control of ship pressure reports follows the approach of Sanders (1991) to screen mislocated reports, miscoded data, and biased surface pressure observations.

The preprocessing of the data stream also includes the adjustment of all measurements/observations of the marine surface wind to a common averaging interval, reference height, and to equivalent neutral boundary layer stratification. The intent of the analysis is to resolve the "synoptic scale" wind field at 3-h intervals on a grid of spacing 0.5° in latitude and longitude covering the analysis domain. To minimize the effect of "mesoscale" variations on the buoy measurements, hourly samples of the 8.5-min average wind are smoothed by averaging three successive measurements with weights 0.25, 0.5, and 0.25. For the buoys that obtained continuous 10-min averages, an hourly average wind is obtained directly by averaging six successive 10-min averages. The averaging is done on meridional and zonal wind components of the wind to derive average wind direction and on the scalar wind speed to derive average wind speed.

Canadian buoy vector average wind speeds are first transformed to effective scalar average winds using a wave height dependent factor. Gilhousen (1987) has suggested that the underestimate of the scalar wind by vector averaging for a sample of data from U.S. buoys is about 7% for wind speeds greater than 8 m s^{-1}; this result was derived from analysis of measurements in rather moderate sea states (HS less than about 5 m). However, the underestimate may be greater in higher sea states, and in fact forecasters in Canada tend to regard the Canadian buoy reported gust value as a better measure of the average wind at standard height in storm conditions. (The buoy records and transmits the highest running 8-s mean gust.) This impression was also formed by the kinematic analysts in this study, after comparing winds to ship reports and winds derived from pressure gradients using a calibrated boundary layer model. A comparison of the dependence of the gust factor (reported gust speed/reported average speed) on reported HS for Canadian and U.S. buoy observations in the HOS (shown in Fig. 2) does suggest a dependence of vector-averaged speed on sea state, which does not appear for scalar-averaged winds. Assuming that the gust factor itself should not depend on sea state (and hence that the scalar-based factor from NOAA buoys is correct) provides a linear (in HS) correction factor (by normalizing the ratio by its base value) for the vector wind speed average, which varies from 4% at HS of 5 m up to 12% at HS of 15 m.

The adjustment of measured scalar (or adjusted vector) average wind speed to a common reference level is carried out following the procedure originally suggested by Cardone (1969) (see also Cardone et al. 1990). The procedure uses stability-dependent surface wind profile laws and an assumed dependence of the roughness parameter on wind speed, to calculate an "effective neutral" wind speed at a reference height. The effective neutral wind speed U_e is the "virtual" wind speed that at height z_e imparts, in neutral thermal surface boundary layer stratification and for the assumed drag law, the same stress as imparted by the measured, U_m, measured at height z_m in a thermally stratified boundary layer:

$$U_e = U_m \frac{\log(z_e/z_0)}{\log[z_m/z_0 - \psi(z_m/L)]}, \qquad (1)$$

where L is the Monin–Obukhov length and ψ is the "profile" stability function [for a more detailed description of the iterative procedure used to calculate U_e from the three known quantities: measured wind speed, measurement height, and air–sea temperature difference, see Cardone (1969) or Ross et al. (1980)]. The calculation also yields estimates of the friction velocity U_* and roughness length z_0. Oceanweather, Inc. (OWI) use the effective height of 20 m, so that buoy winds can be compared in an analysis to winds reported by ships.

Ship reported winds are converted to 20-m "effective neutral" winds for input to the wave models following the procedures also described by Cardone et al. (1990), where adjustments are made depending on whether the wind was estimated or measured, and the height of the anemometer where applicable (and known, from the World Meteorological Organization List of Supplementary and Selected Ships). If the anemometer height was not known, then an estimate was made based on average heights. Where the wind speed was estimated according to the Beaufort scale, Cardone et al. (1990) determined the effective neutral speed from the relationship $V_{20} = 2.16V_r^{7/9}$, where V_r is the reported wind speed. No attempts were made to otherwise correct the winds from the voluntary observing fleet (VOF), such as possible flow distortion effects.

There are two additional subtle and related assumptions implied in the adjustment procedure. The first is that the roughness parameter does not depend on wave

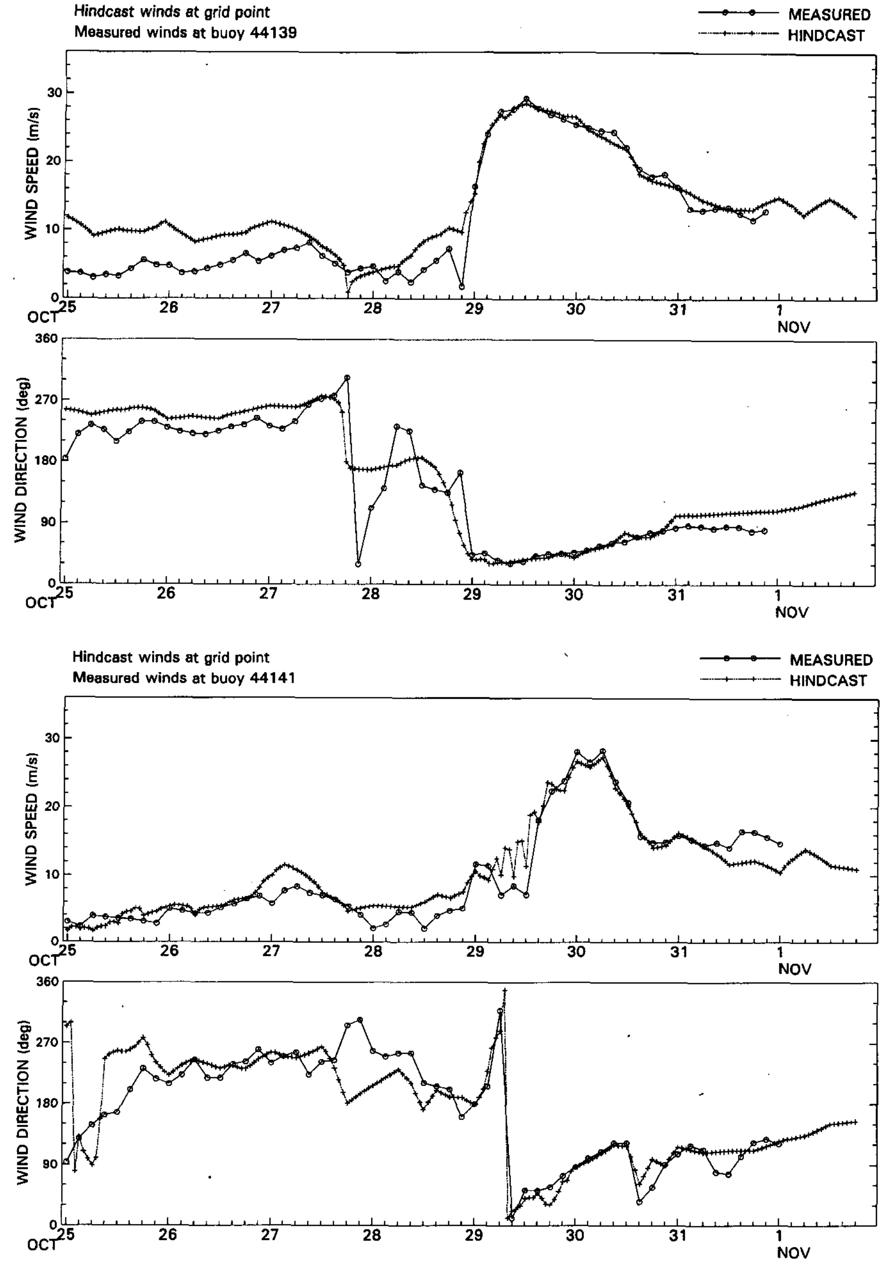

FIG. 6. Comparison of analyzed and buoy time histories of 20-m effective neutral wind speed and direction at four (a)–(d) buoys in the Halloween storm. Hindcast winds based on kinematic analysis only after 1200 UTC 28 October 1991.

age, but a number of recent studies (e.g., Maat et al. 1991) suggest that it does. To account for this effect would have required making the wave hindcast a part of the wind analysis process itself.

The second assumption is that normalizing the effect of thermal stratification through the friction velocity U_* as is implied in the adopted procedure, also accounts for the effect of stability on the wave generation process itself. However, as suggested by Kahma and Calkoen (1992) scaling of wave growth with fetch in terms of nondimensional variables scaled with U_*, as opposed to U_m, appears to be insufficient to fully explain the effects of thermal stratification of the surface boundary layer on wave development with fetch.

2) BOUNDARY LAYER MODEL SURFACE WINDS

An initial estimate of the 3-hourly wind field throughout the analysis domain is made using a marine planetary boundary layer model (MPBL) applied to

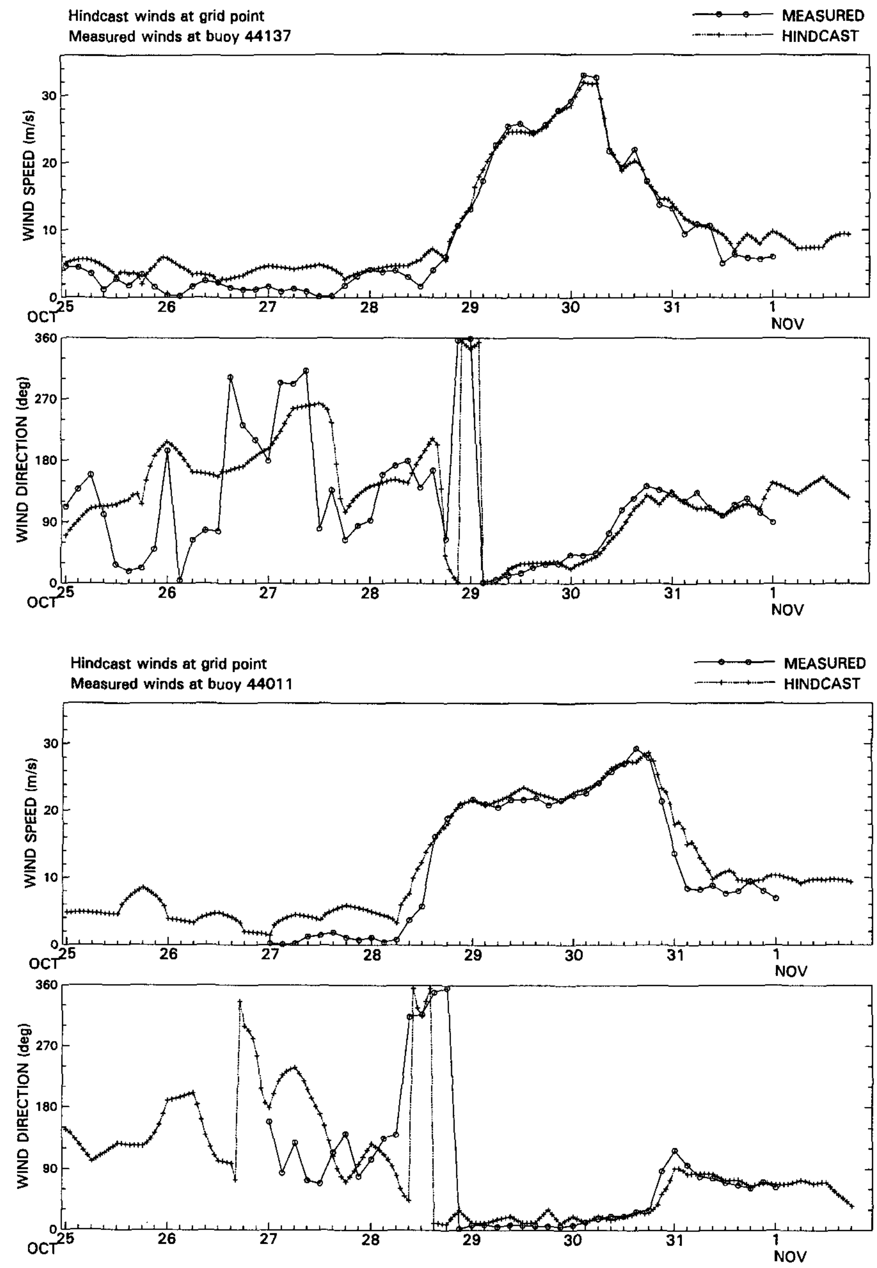

FIG. 6. (*Continued*)

gridpoint-specific gradients of sea level pressure, air temperature, and air–sea temperature difference. Since its development (Cardone 1969), this particular model has been used at many national centers for routine analysis and forecasting and in many studies (see, e.g., Overland and Gemmill 1978; Cardone 1991). For this application, the required MPBL variables were derived from carefully hand-analyzed and digitized maps drawn to carefully maintain continuity of centers of action and fronts. A large number of evaluations of surface wind fields produced in this manner (Cardone 1991) indicate that a scatter of about 3 m s^{-1} in wind speed and 30° in wind direction is about the intrinsic limit of skill in specification of synoptic-scale surface wind fields over the ocean using simple analytical steady-state MPBL models. To reduce this error in a surface wind analysis scheme requires the assimilation of measured surface wind data.

3) KINEMATIC ANALYSIS

Kinematic analysis (KA) is carried out only for the most critical parts of the wind field. This criteria gen-

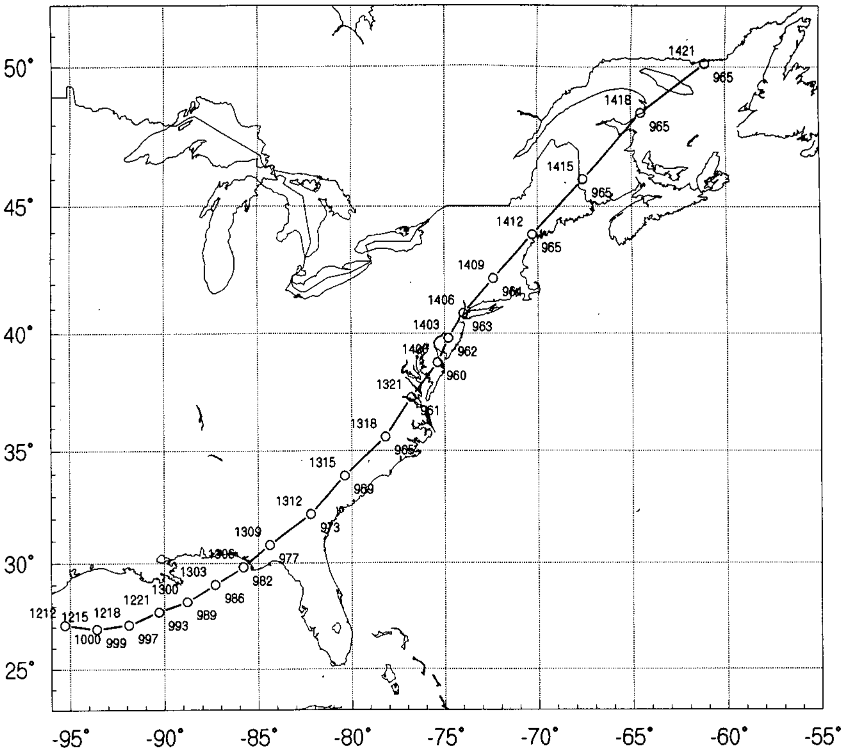

FIG. 7. Track and central pressure of the storm of century.

erally excludes the model spinup period (generally the first 36–72 h of the modeled period), areas well outside the circulations of the major cyclonic centers of action and also over the open North Atlantic Ocean well east of the buoy array, where the sparsity of ship data tend to minimize any incremental skill to be gained from KA. In KA, streamlines and isotachs of the effective neutral 20-m wind are manually drawn at 3-h intervals, subsequently hand-digitized at 0.5° latitude–longitude intervals, and where available they simply supersede the MPBL gridpoint winds. The KA winds blend smoothly with the MPBL on the borders of the KA region because they are drawn to do so by the KA analyst.

b. *Evolution of the wind field*

1) HALLOWEEN STORM

The HOS has been studied heretofore mainly in terms of the devastating impact of its storm surge and heavy swell on the coastal communities from Maine (where, e.g., U.S. President Bush's Kennebunkport home sustained severe damage from wave action) to as far south as the U.S. Virgin Islands. The storm damaged or destroyed over a thousand beach front homes, caused 12 deaths (including five in a fishing boat loss offshore) and insured losses in the United States estimated at between $1.5 and $2 billion (NOAA 1992).

The evolution of the main meteorological systems comprising the HOS event have been described in detail by Cameron and Parkes (1992) using mainly operational analyses produced at AES, and by NOAA (1992), using mainly NOAA National Meteorological Center (NMC) products. The emphasis here is on the surface wind field evolution associated with the formation movement and interaction of the two cyclones comprising this event, one subtropical and the second extratropical. Figure 3 shows the tracks of these systems over the period of interest. Figure 4 is a composite of the surface wind fields over the subdomain of the analysis grid shown, at 24-h intervals over the period 0000 UTC 25 October–0000 UTC 1 November 1991. The conventional wind barbs representing the 1-h average 20-m wind are plotted at 1° spacing.

The southern subtropical system formed late on the 25th about 300 nm south of Bermuda, intensified to tropical storm strength early on the 26th and hurricane strength (Grace) late on the 26th. Grace moved slowly northwestward on the 27th. The surface wind field about Grace during this period was characterized by winds of gale to storm force over a large area, up to 300 nm from the center. Grace slowed and turned northward on the 28th while weakening, then turned toward the east and moved for a time eastward toward Bermuda early on the 29th. While the storm was losing its tropical characteristics and its inner core of near hurricane force winds (not well resolved on the 0.5° grid) it still at this time possessed a large circulation with winds in excess of 20 m s^{-1} covering the large area shown in Fig. 4. Late on the 29th, the remnants of Grace turned northeastward, sparing Bermuda significant impact, and on 30 October became absorbed into the northern cyclonic system.

The northern system formed out of a weak wave that had been moving eastward out of New England along a strong basically east–west-oriented cold front laid out along the St. Lawrence Valley early on the 27th. As the wave reached the eastern tip of Nova Scotia at about 1200 UTC on the 28th, it evidently turned abruptly southward and began to intensify rapidly. Twenty-four hours later, the center was near 41°N, 55°W, its central pressure having fallen about 24 mb. The cyclone then turned toward the west-southwest and continued to intensify over the next 24-h during the 30th, before slowing and filling on the 31st. The center executed a counterclockwise loop on the 31 October and 1 November while filling. Beyond 1 November, the cyclone turned northward and for a time intensified and acquired tropical characteristics before weakening and entering Nova Scotia just west of Halifax on 2 November.

The surface wind field about the northern system intensified rapidly late on the 28th, first in the northern and western quadrants of the circulation. By early on the 29th, surface winds of greater than 25 m s^{-1} developed from the Grand Banks of Newfoundland southwestward, and a continuous northerly airstream of surface winds of 20 m s^{-1} or greater extended over the western parts of the two cyclones. East of the two cyclones, the circulations remained distinct at this time. The details of the interaction of Grace and the extratropical cyclone (EC) on the 30th may never be completely resolvable since there was no aircraft reconnaissance of Grace after this time. The NOAA National Hurricane Center (NHC) analyses carried a distinct circulation of Grace until 1800 UTC 29 October after which NHC considered its circulation absorbed into the northern system. Our kinematic analysis supports the survival of a distinct circulation center of the remnants of Grace until at least 0600 UTC 30 October. Regardless of the exact evolution of the center, however, there appears little doubt that the tropical system was responsible for the northward migration of a band of gale force southerlies east of the center of the southern system and toward the frontal boundary associated with the northern system. By 0000 UTC 31 October, the wind field has simplified into the pattern of an extensive circulation about a single center (hence the "Halloween storm") located just south of Georges Bank.

The strongest surface winds in the HOS, up to 33 m s^{-1}, occurred between 0000 and 1200 UTC, and were found north of the northern system, in the area of the most intense pressure gradients. At 1200 UTC 30 October there was a total pressure drop of 60 hPa between the 972-hPa low near 40°N, 62°W and the 1042-hPa anticyclone centered near 50°N, 65°W, with over two-thirds of this gradient concentrated between the low center and the southwest tip of Nova Scotia.

The availability of the Canadian buoy winds and ship reports allowed the KA to detect fine structure usually not resolved, in the evolution of the surface winds in the airstream north of the cyclone prior to and during the occurrence of the maximum sea states in the Canadian buoy array. This fine structure is shown in the composite of KA covering the period 0600 UTC 29 October and 1800 UTC 30 October given in Fig. 5. (The 3-h KA are sampled at 12-h intervals in this figure.) The broad area of greater than 50 kt wind speeds north of the storm center during this period is actually a combination of two distinct wind maxima, which could be tracked southwestward during this period. The first maximum seemed to originate near 45°N, 51°W at 0600 UTC 29 October and to propagate west-southwestward at about 20 m s^{-1}, as estimated from its movement over a 12-h period. The core of this feature passed almost directly over 44139 inducing the indicated speed maximum of 29 m s^{-1} (at 20-m height) at 1200 UTC as seen in the time history of measured winds at that buoy in Fig. 6a. This feature, which we shall call a surface wind "jet streak" or HOS-JS1, lost definition after 1800 UTC 29 October and was overtaken by a second JS, HOS-JS2, which developed upstream near 45°N, 52°W at 1500 UTC 29 October. HOS-JS2 could be tracked west-southwestward a little south of the track of HOS-JS1, the core speed maximum of 33 m s^{-1} passing just north of 44141 between 0000 and 0300 UTC 30 October and passing directly over 44137 at 0300 UTC 30 October, as reflected in the measured time histories in Figs. 6b and 6c. The time history at 44137 also shows a secondary speed maximum at 0900 UTC 29 October, which is the effect of the core of HOS-JS1 passing north of this site earlier. HOS-JS2 maintained its identity over a longer period than HOS-JS1, roughly the 48-h period 1500 UTC 29 October–1200 UTC 31 October. This JS propagated down the flow at an average speed of about 17 m s^{-1} as it approached and passed 44137. This speed is about 50% faster but basically in the same direction as the movement of the parent low center during this period. By 1200 UTC 31 October, HOS-JS2 seemed to become associated with the parent low and propagate slowly westward with it thereafter as the maximum core wind speeds gradually diminished. Figure 6d shows the arrival of the core of this JS over 44011, now associated with northerly rather than east-northeasterly flow late on 30 October. These interesting finescale features of the wind field seem to be intimately related to the pattern of extreme wave generation observed in the Canadian buoy array and will be discussed in the next section.

2) STORM OF THE CENTURY

The SOC is one of the greatest weather catastrophes ever to affect the United States. The death toll of 270

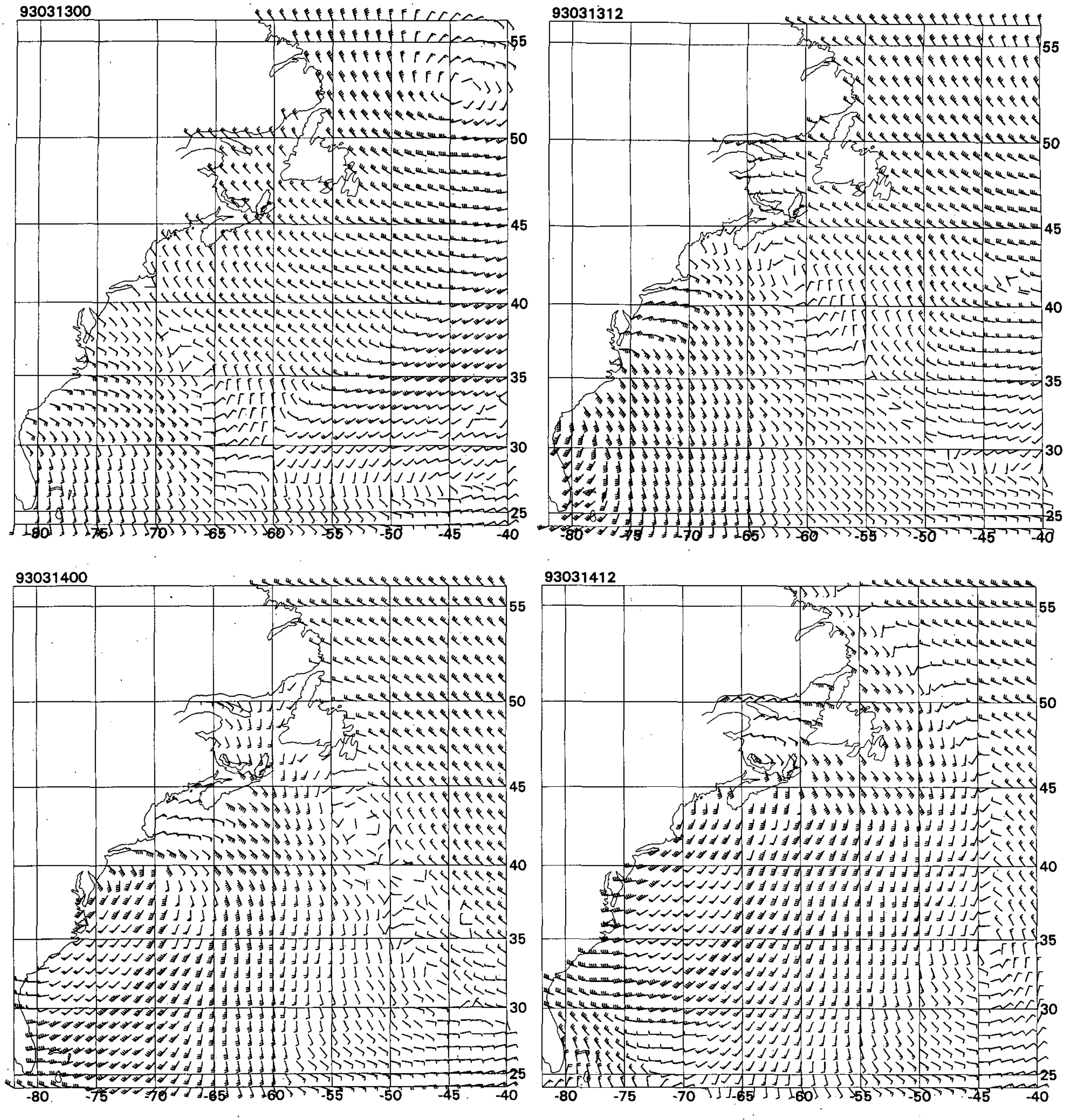

FIG. 8. Reanalyzed surface wind fields in the storm of the century at 12-h intervals (a)–(f), 0000 UTC 13 March–1200 UTC 15 March 1993. Wind barbs represent effective neutral 1-h average wind speed at 20-m height (kt).

exceeded the combined death toll of Hurricanes Andrew and Hugo by three times. Insured losses were estimated at $6 billion. While the impact of SOC is usually expressed in terms of its associated blizzard conditions and record snowfalls from Alabama to Maine, the extreme surface winds and low temperatures and the property loss on land (e.g., NCDC 1993b), the impact at sea was also great. At least 48 lives were lost at sea, including all hands on the bulk carrier *Gold Bond Conveyor* south of Halifax on 15 March.

The SOC was foreseen a week in advance by NOAA medium-range numerical weather prediction (NWP) models and very well forecast by short-term NWP models. Figure 7 shows the track of the surface low. The surface development began over the western Gulf of Mexico early on 12 March 1993, and intensification

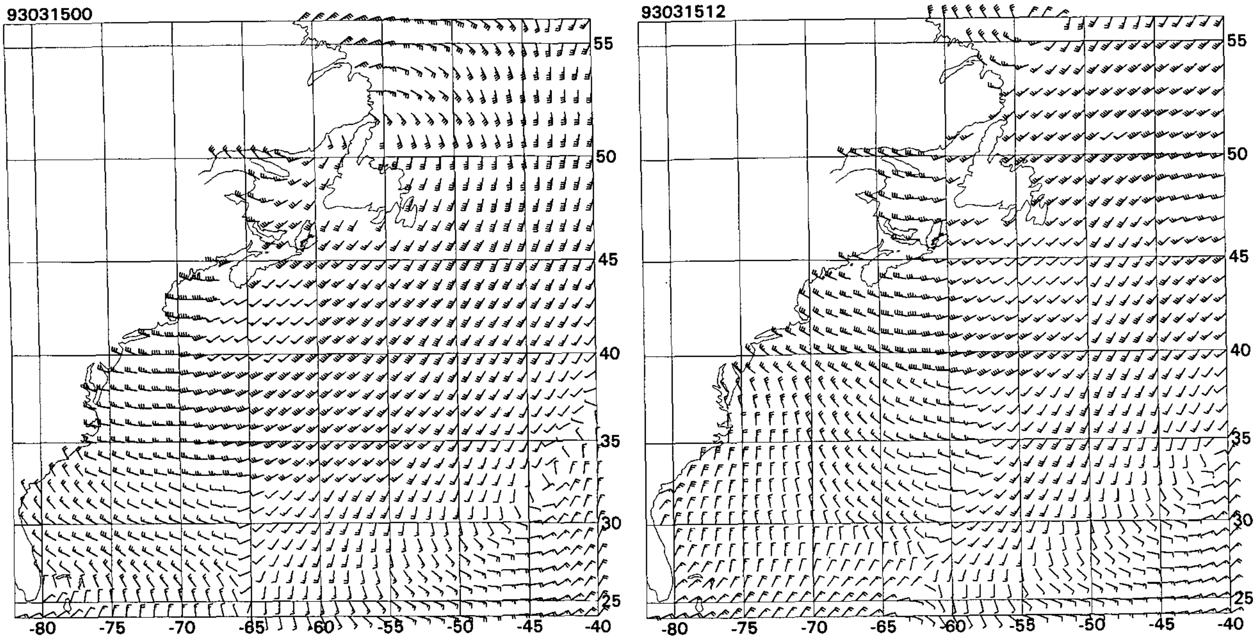

FIG. 8. (*Continued*)

was explosive from the beginning. The central pressure decreased from 1000 to 969 hPa in the 24-h period during which the storm crossed the northern Gulf of Mexico and entered Georgia. Even in the Gulf of Mexico the storm developed its "100-year" signature. The storm generated wind gusts to 98 mph on South Timbalier platform south of Louisiana. The maximum HS at NOAA buoy 42003 (25.9°N, 85.9°W) was measured at 9.2 m.

Figure 8 shows the evolution of the wind field at 12-h intervals between 0000 UTC 13 March and 1200 UTC 15 March. The full cyclonic circulation is not shown on these plots because winds over land are not plotted, and the center remained on the coastal plain as it moved rapidly northeastward. All of the extreme wave generation occurred in the basically southerly (southeast to southwest) wind field in the Eastern Hemisphere of the circulation. These strong winds crossed the Florida Peninsula and emerged off the southeast coast (Figs. 8a and 8b) early on the 13th. By 0000 UTC 14 March, surface winds (1-h average at 20 m) attained maximum speeds of 30 m s^{-1} east of the Carolinas. These winds reached the Scotian Shelf about 24 h later. The lowest central pressure recorded on land was 958.4 mb at White Plains, New York, though a ship docked in Baltimore Harbor recorded 956 mb. The central pressure increased and the maximum winds gradually weakened as the storm moved through the Canadian Maritimes on the 15th.

At least over the main part of the intense circulation that passed over the buoy array off the East Coast, the KA allowed the resolution of several finescale structures including two well-defined JS. The more energetic JS of the two, termed here SOC-JS1, emerged off the northeast coast of Florida late on the 13th, and accelerated northeastward during the 14th and 15th, as shown in the composite of KA (sampled at 6-h intervals) in Fig. 9. The movements of these features dominate the time histories of the measured winds at the buoys in their paths, as shown in Figs. 10a–d, which compare modeled and measured surface winds (again the measured winds are smoothed from three consecutive hourly measurements, adjusted to 20-m neutral stability) at buoys 41006, 41002, 44004, and 44137. The core of SOC-JS1 with maximum winds of 30 m s^{-1} passed just north of buoy 41006 inducing a maximum wind speed of 25 m s^{-1} there at 1800 UTC 13 March, then passed apparently right over 41002 at 2100 UTC 14 March where maximum winds speeds were 30 m s^{-1}, just east of 44004 at 0600 UTC 14 March (maximum wind speeds of 25 m s^{-1}), and just west of 44137 at around 2100 UTC 14 March (maximum wind speeds of 24 m s^{-1}). The propagation velocity of the core of JS1 averaged about 13 m s^{-1} off the east coast of the United States accelerating to 17 m s^{-1} over Canadian waters. A second JS, SOC-JS2, is resolved but not as accurately as SOC-JS1 because it evolved in part over sparse data areas just east of the buoy array. The surface flow was basically southeasterly in this JS, but the JS itself propagated north-northeastward. The core of SOC-JS2 (with maximum winds about 28 m s^{-1}) passed east of 44004 at 2100 UTC 13 March and east of 44137 at 0600 UTC 14 March where the secondary local wind speed maxima are induced as seen as indicated in Figs. 10c and 10d.

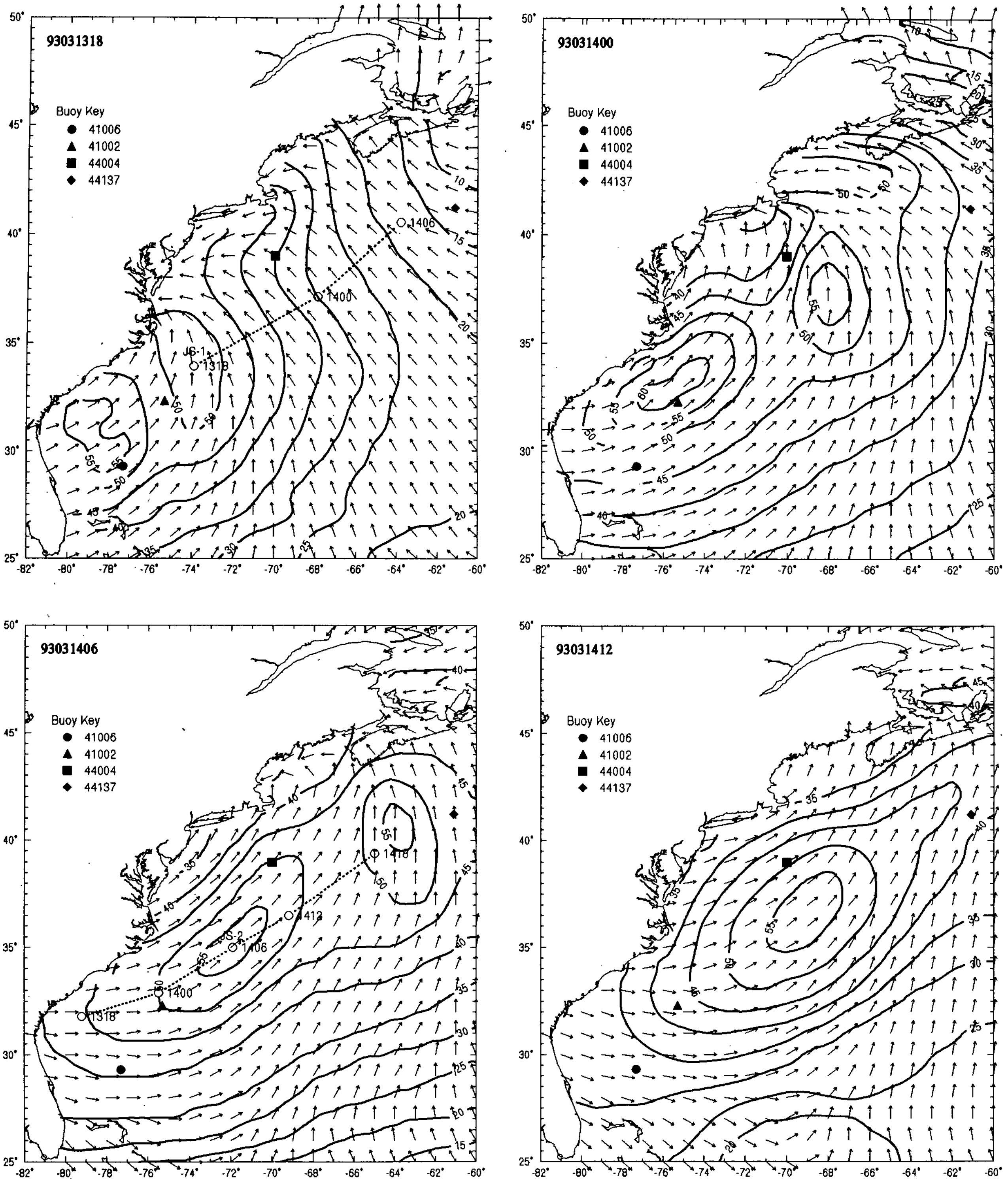

FIG. 9. Six-hour (a)–(d) surface wind field analyses in the immediate vicinity of the storm of the century, showing evolution of major circulation features including jet streaks between 0600 UTC 13 March–0000 UTC 15 March 1993.

4. Wave hindcasts

a. Models

All of the wave models are of the discrete spectral type. This general type of wave model has gradually replaced earlier "significant wave" type models at most (but not yet all) major analysis–forecast centers and has been used in most wave climate assessment studies carried out over the past two decades. In a discretized spectral model, the directional spectrum is resolved at each model grid point in terms of a number of frequency-direction bands and the evolution of the sea state is found by the numerical solution of the spectral energy balance equation, which in deep water with small ambient currents can be written

$$\frac{\partial E}{\partial t} + \nabla\cdot(\mathbf{C}_g E) = S_{\text{in}} + S_{\text{ds}} + S_{\text{nl}}, \qquad (2)$$

where $E(f, \theta, \mathbf{x}, t)$ is the energy density at position $\mathbf{x}$ and time t and is a function of frequency f and propagation direction θ; $\mathbf{C}_g$ is the group velocity vector; S_{in} is the source term for energy input to the spectrum from the atmosphere; S_{ds} is the source term representing dissipative processes; and S_{nl} represents nonlinear energy transfers within the spectrum. The numerical solution of this equation is carried out in separate propagation and source term integration steps. The basic attributes (spectral banding, grid systems, propagation scheme, etc.) of the four models are summarized in Table 2.

1) OWI1G

The source-term representation of this model, also known as ODGP, was developed originally by Pierson et al. (1966, hereafter PTB) and was later modified and retuned to provide accurate specification of directional wave spectra in tropical cyclones (Cardone et al. 1976). The ODGP variant of PTB was later found to work equally well in a wider range of meteorological regimes (Reece and Cardone 1982). In ODGP, separate source terms for S_{in}, S_{ds}, and S_{nl} are not resolved but are replaced by an algorithm that leads to at first linear and then exponential growth of spectral energy. The growth algorithm is designed to allow the spectrum to gradually approach the Pierson–Moskowitz (PM) fully developed spectrum at long fetch or duration under the action of a steady wind. The spectral growth algorithm was later modified (ODGP2, see Khandekar et al. 1994) when an "equilibrium-range relaxation" was added following the model of Resio (1981) to allow the high-frequency tail of the spectrum to adjust to the stage of wave development (a consequence in nature of the balance between three source terms in the high-frequency tail of the spectrum). The propagation scheme (Greenwood et al. 1985) is a downstream interpolatory scheme that is rigorously energy conserving with great circle effects included. The ODGP2 growth and propagation schemes are the basis of the global wave model (GSOWM) operated by the U.S. Navy Fleet Numerical Meteorology and Oceanography Center (FNMOC) from 1985 until mid-1994 (Clancy and Sadler 1992), when WAM was implemented for operational dissemination, and of models used in proprietary and public domain wave climate assessment studies for numerous basins worldwide (e.g., Cardone and Ewans 1992; Swail et al. 1992; Eid et al. 1992).

2) Resio2G

This second-generation model, also known as WAVAD, evolved from an earlier 2G model first described by Resio (1981). The source terms currently used are described in Resio and Perrie (1989). In WAVAD, S_{in} is a tuned quadratic function of dimensionless peak frequency (Uf_m/g). Nonlinear source term S_{nl} is modeled in terms of its effective energy transfer onto the forward face of the spectrum. The form for this transfer was determined from calculations of the total flux of energy to the forward face, which is expressed in terms of the migration of the peak spectral period toward lower frequencies; S_{ds} is based upon the assumption that wave breaking removes all energy that is input to or transferred into frequencies above some threshold frequency. The propagation of spectral component energy is by finite differences using a first-order upstream differencing scheme. Model evaluation can be found, for example, in Hubertz et al. (1993). This model is currently used by the U.S. Army Corps of Engineers in its Wave Information Study (WIS) and is used by several private companies worldwide.

3) WAM4

This is the fourth cycle of the third-generation model (WAMDI) originally described by WAMDI Group (1988). In WAM each source term is specified explicitly and the source-term balance is integrated to yield the net development of the spectrum over a time step of integration without arbitrarily forcing of spectral shape or specification of an external limit to growth. However, in the original development of the model, considerable experimentation with and tuning of the input and dissipation source terms was carried out (Komen et al. 1984) to achieve growth rates and asymptotic behavior under constant winds in agreement with field data. The present version uses the input source terms described by Janssen (1991). The most important difference between basic WAMDI and WAM4 is that the growth rate is computed not only in terms of the wind alone (as in all of the other models applied here) but is also is allowed to vary as a function of the stage of wave development. The input S_{in} is basically quadratic in the friction velocity U_* and since U_* is a

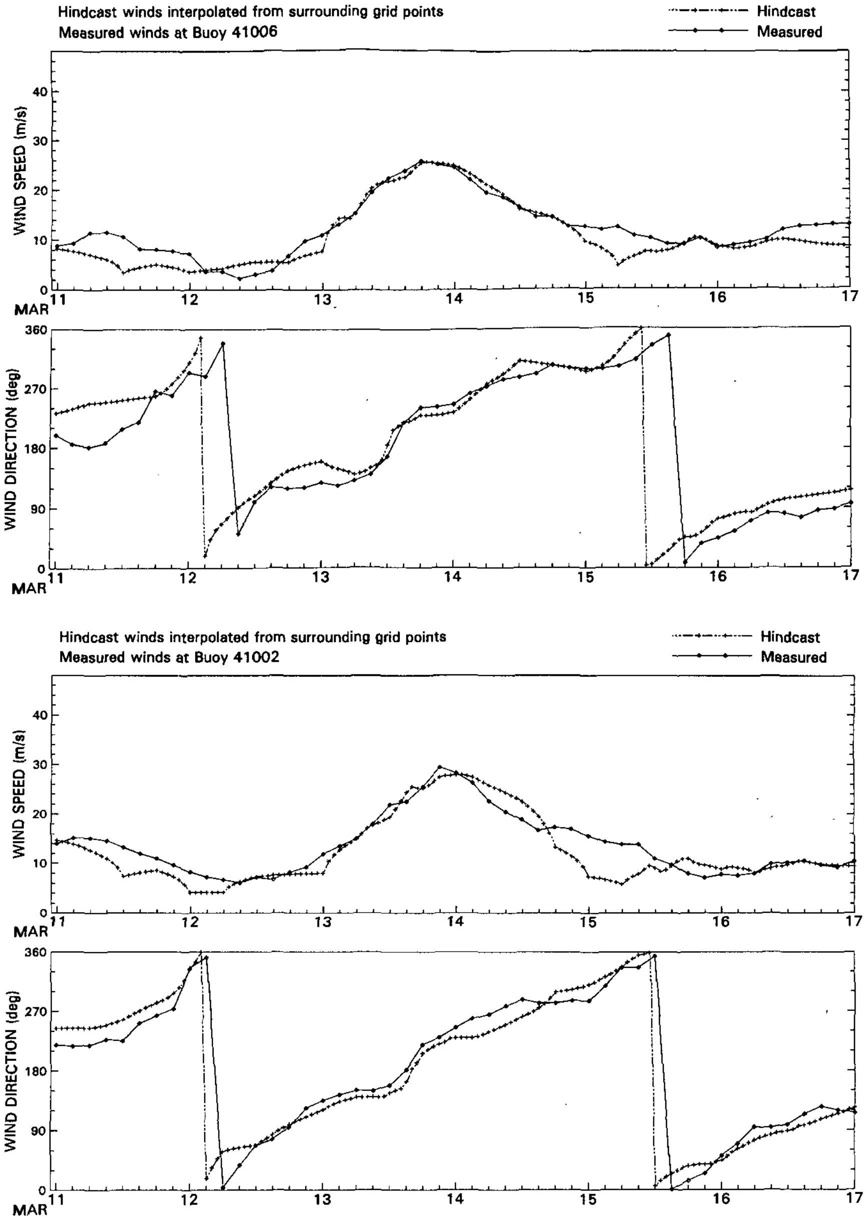

FIG. 10. Comparison of analyzed and buoy time histories of 20-m effective neutral wind speed and direction at four (a)–(d) buoys in the storm of the century. Hindcast winds based on kinematic analysis only after 0600 UTC 13 March 1993.

function of roughness parameter, which is itself a function of sea state, the wave and wind fields are weakly coupled. Also, whereas in WAMDI the whitecapping dissipation source term (Hasselmann 1974) is quadratic in frequency, in WAM4 it is proportional to the fourth power of frequency. Here S_{nl} is a parameterization of the exact nonlinear interactions as proposed by Hasselmann (1985). This so-called discrete interaction approximation (DIA) is described in WAMDIG (1988). Propagation is by first-order finite differencing.

4) OWI3G

This model consists of a source term representation and integration scheme based upon WAMDI combined with the propagation scheme used in OWI1G. The source terms follow the theoretical forms used in WAMDI but with different numerics and code and with the following modifications. First, a linear excitation source term is added to S_{in}, taken as a downscaled variant of the term used in ODGP. This allows the sea to grow from a flat calm initial condition in OWI3G, un-

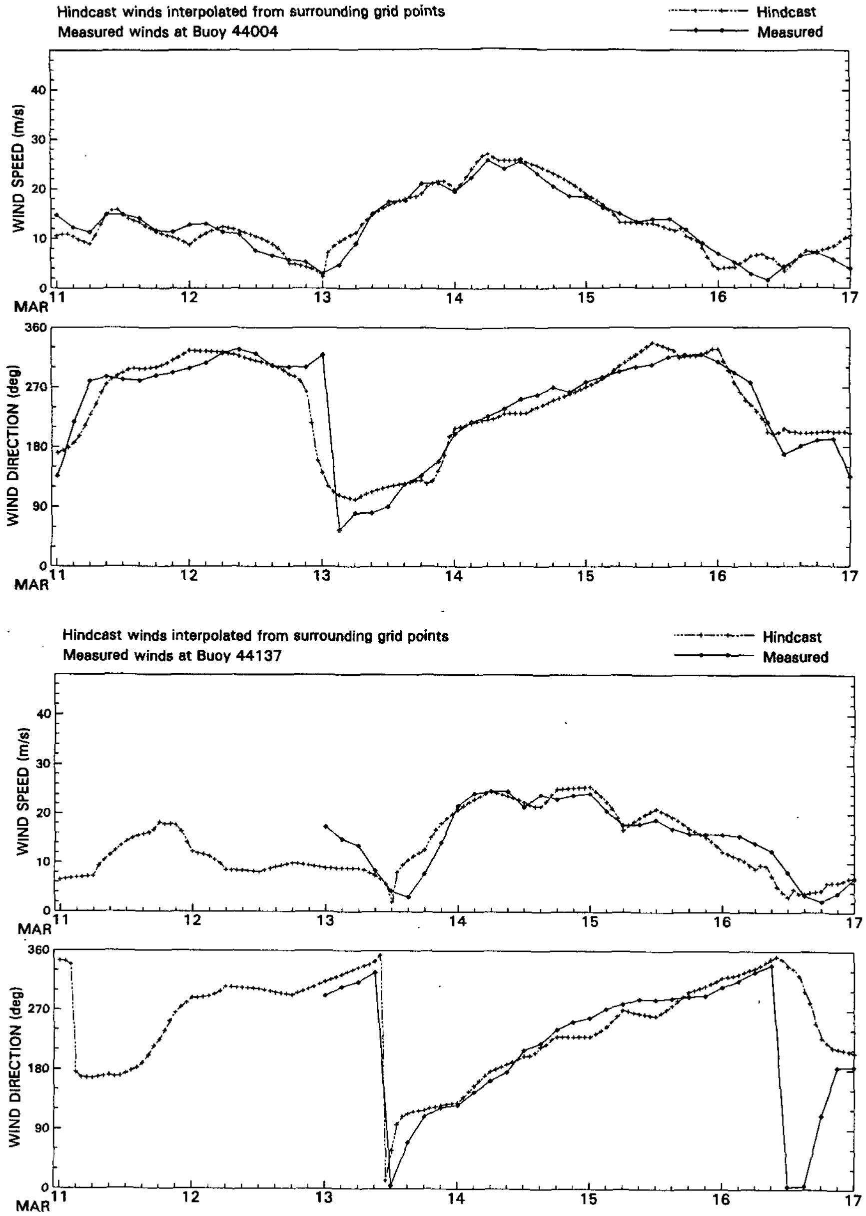

FIG. 10. (*Continued*)

like all cycles of WAM, which require an artificial warm start from a prescribed initial spectrum. The exponential input term is the empirical form of Snyder et al. (1981) in which S_{in} is taken as a linear function of U_*. However, unlike WAMDI in which U_* is computed from U_{10} following the drag law of Wu (1982), in OWI3G, a different drag law is used in the model tuning stage. That drag law follows Wu closely up to about 20 m s^{-1} and then becomes asymptotic to a constant at hurricane wind speeds. Dissipation S_{ds} is also taken from WAMDI except that the dependence on frequency is cubic rather than quadratic. Finally, for S_{nl}, the DIA is adopted except that two modes of interaction are included (in WAMDI the second mode is ignored). The modifications just described were adopted and refined based upon tuning runs against the fetch-limited growth benchmark for 20 m s^{-1} wind speeds under constant winds used to tune WAMDI initially, as well as in repeated trial hindcasts of a well-documented moderate extratropical cyclone (SWADE IOP 1) and two intense Gulf of Mexico hurricanes (Camille 1969; Frederic 1979).

TABLE 2. Wave model attributes.

	Spectral discretization				Grid system				Time step (s)	
	Frequency		Direction							
Model	No.	Width	No.	Width	Domain	Spacing	Source terms	Propagation	Source	Prop
OWI1G	23	$\Delta f/f = 0.1$	24	15°	C: 24°–67°N 30°–82°W F: 24°–50°N 52°–82°W	2° 0.5°	Cardone et al. (1976)	First-order interpolatory	900	900
Resio2G	15	$\Delta f = 0.01$	16	22.5°	C: 24°–67°N 30°–82°W F: 35°–51°N 54°–82°W	1° 0.5°	Resio and Perrie (1989)	First-order finite diff.	3600	3600
WAM4	26	$\Delta f/f = 0.1$	24	15°	C: 23°–67°N 30°–82°W	0.5°	Gunther et al. (1991)	First-order finite diff.	600	600
OWI3G	23	$\Delta f/f = 0.1$	24	15°	C: 24°–67°N 30°–82°W F: 24°–50°N 52°–82°W	2° 0.5°	Khandekar et al. (1994)	First-order interpolatory	900	900

C: coarse nest; F: fine nest; No.: number of bands.

b. Model grids and output

A basic grid constraint was that at least within the general domain of the buoy array (say 30°–45°N, 50°–80°W, see Fig. 1) all models use a grid spacing 0.5° in latitude and longitude. This ensured that resolution effects would not contribute to *differential* behavior between the different wave models in the energetic parts of these storms and that the wave model grid point selected to represent a buoy would be the same for all models. As shown in Table 2 most models adopted a two-nest grid layout to satisfy this constraint.

Since only deep-water physics was considered in the propagation and source terms of the model used, model results are compared to measurements from buoys moored in deep water, or basically those shown in Fig. 1. These include buoys 44008 and 44011, which are in marginally shallow water. Comparisons were made at these buoys in HOS only because of the high sea states observed there, but separate comparison statistics were computed for strictly deep water buoys as well. For each run, hourly time histories of the directional spectra were saved at the closest agreed model grid point to each buoy. These were reduced to the following integrated properties of the spectrum:

$$E(f) = \int_0^{2\pi} E(f, \theta)\, d\theta \tag{3}$$

$$\mathrm{HS} = 4\left[\int_0^{2\pi}\int_0^{\infty} E(f, \theta)\, df\, d\theta\right]^{0.5} \tag{4}$$

$$T_p = f_p^{-1} \tag{5}$$

$$\mathrm{VMD} = \tan^{-1}\frac{\displaystyle\int_0^{2\pi}\int_0^{\infty} \sin\theta E(f, \theta)\, df\, d\theta}{\displaystyle\int_0^{2\pi}\int_0^{\infty} \cos\theta E(f, \theta)\, df\, d\theta}. \tag{6}$$

In Eq. (5), f_p is derived from a parabolic fit to the equation $dE(f)/df = 0$. VMD is the vector mean direction.

5. Evaluation of alternative hindcasts

An objective evaluation of the accuracy of the common wind field is not possible in terms of measured winds because every wind observation and measurement had to be used in the wind field analysis process. Figures 6 and 10 contrast the difference in skill at the buoy locations at least, between wind fields computed from the pressure field and stability using a boundary layer model (as shown by the comparisons for times outside the KA periods) and wind fields derived by KA, which relies on observations. However, as shown in the comparative analysis of alternative wave hindcasts with WAM4 driven by six different wind fields in the study of SWADE IOP 1 (Cardone et al. 1994), the KA wind field used is probably the most accurate wind field derivable from the available database. We caution, however, that since the KA weights the buoy in situ wind measurements so heavily, there remains the possibility that the wind speed fields may still be biased at the higher sea states even after our corrections for the height, stability, and averaging method if the ability

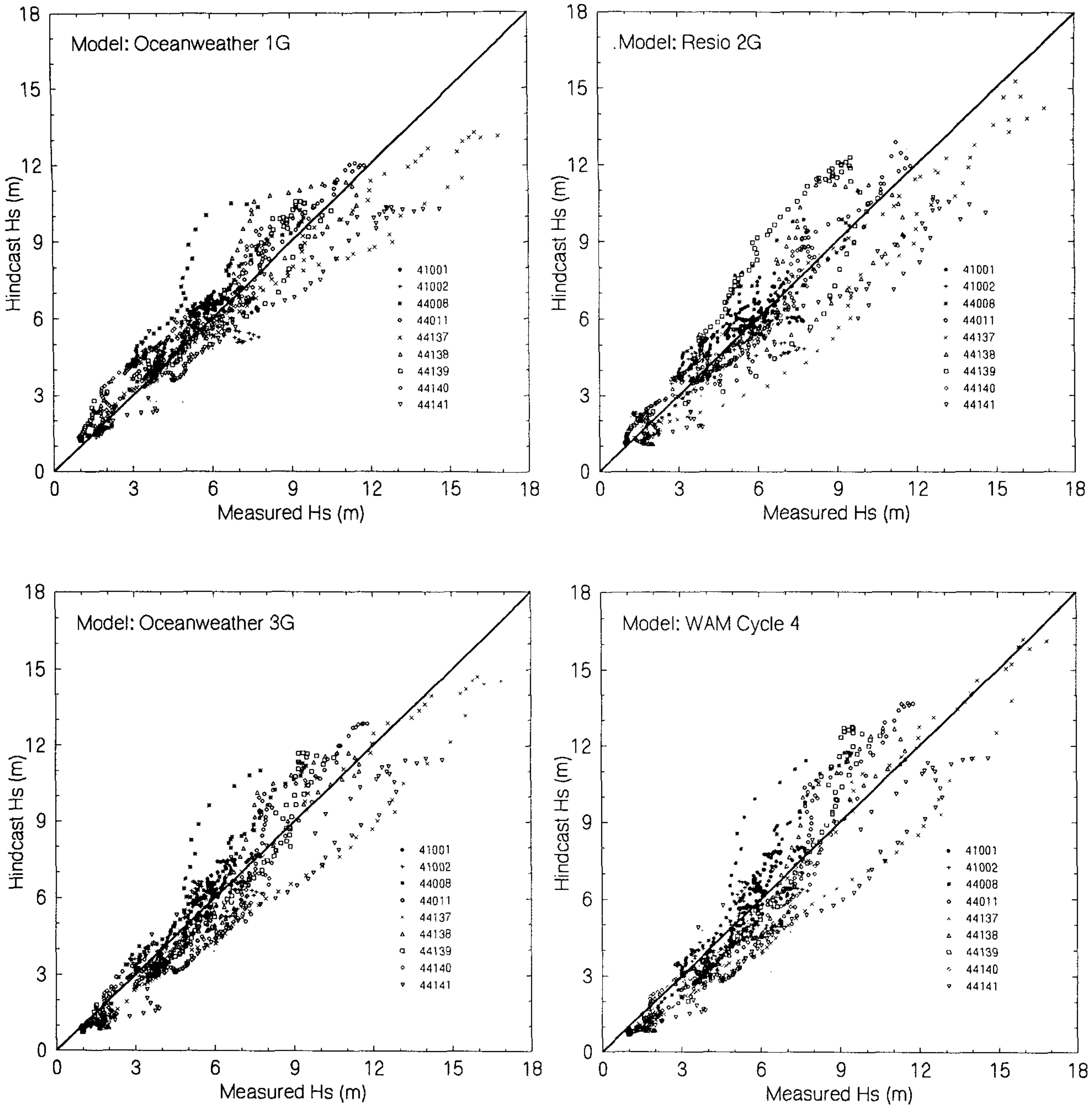

FIG. 11. Comparison of 3-h hindcast and measured wave height at 9 buoys in the Halloween storm for four wave models.

of the buoy to measure winds is somehow impaired in extreme seas.

Except for the adjustment of the measured vector-averaged winds at Canadian buoys, the buoy wave measurements were not used in the hindcasting process and therefore may be used to objectively evaluate the alternative wave model hindcasts. To effect this comparison the following statistics were computed on significant wave height and peak spectral period in a series of n measurements m, and corresponding hindcasts h:

mean of measured and hindcast

$$\bar{m} = \frac{1}{n} \sum_i m_i \tag{7}$$

$$\bar{h} = \frac{1}{n} \sum_i h_i; \tag{8}$$

TABLE 3. Comparison statistics of 3-h measured and hindcast wave height and period at buoys in the Halloween storm for four wave models.

	Significant wave height (m)									Peak period (s)								
Buoy	No. pts	Avg meas	Avg hind	Mean diff	rms diff	Std dev	SI	*R*	CC	No. pts	Avg meas	Avg hind	Mean diff	rms diff	Std dev	SI	*R*	CC
OWI1G																		
41001	108	5.74	6.05	−0.31	0.60	0.52	0.09	0.18	0.85	108	13.25	13.38	−0.13	**1.63**	**1.62**	**0.12**	**0.48**	**0.85**
41002	98	5.11	5.37	−0.27	1.04	1.01	0.20	0.26	0.63	98	14.23	13.40	**0.83**	**1.27**	**0.97**	**0.07**	0.82	**0.94**
44008	108	5.19	6.21	−1.02	1.39	0.95	**0.18**	0.12	0.92	103	11.65	12.02	−0.37	2.57	2.54	0.22	**0.50**	**0.61**
44011	105	6.25	6.56	−0.31	**0.59**	**0.50**	**0.08**	0.26	**0.99**	105	12.70	11.59	1.11	1.90	1.54	0.12	0.80	0.84
44137	108	6.74	5.98	0.76	1.42	1.21	0.18	0.69	**0.99**	108	12.48	10.99	1.49	1.93	1.23	0.10	0.91	0.93
44138	108	4.99	5.29	−0.30	0.87	0.81	**0.16**	**0.41**	0.96	108	10.91	10.53	0.39	**1.82**	**1.78**	**0.16**	0.58	**0.81**
44139	108	5.37	5.69	−0.32	**0.69**	**0.62**	**0.12**	0.28	**0.98**	108	11.02	10.21	**0.81**	**1.70**	**1.49**	**0.14**	**0.63**	0.87
44140	108	4.23	4.95	−0.72	0.89	0.54	**0.13**	0.15	**0.97**	108	11.77	11.06	**0.71**	**1.89**	1.75	0.15	**0.59**	0.58
44141	108	5.93	5.05	**0.89**	**1.46**	1.16	0.20	**0.75**	**0.98**	108	11.32	10.13	**1.19**	**1.81**	1.36	0.12	**0.83**	0.90
All	954	5.51	5.68	−0.17	1.05	1.04	0.19	0.34	**0.94**	954	12.13	11.46	0.67	**1.87**	**1.74**	**0.14**	0.68	**0.83**
Deep	746	5.45	5.48	**−0.04**	1.04	1.04	0.19	0.61	0.94	746	12.11	11.36	0.75	**1.74**	**1.57**	**0.13**	0.31	**0.87**
Resio2G																		
41001	108	5.74	5.89	**−0.15**	0.70	0.69	0.12	0.65	0.73	108	13.25	13.29	**−0.04**	2.00	2.00	0.15	**0.52**	0.76
41002	98	5.11	4.96	0.15	1.03	1.02	0.20	0.59	0.61	98	14.23	13.22	1.01	1.76	1.45	0.10	**0.21**	0.87
44008	103	5.19	5.67	**−0.48**	**1.04**	**0.93**	**0.18**	**0.56**	0.90	103	11.65	10.46	1.19	**1.96**	**1.56**	**0.13**	0.25	0.53
44011	105	6.25	6.60	−0.35	0.78	0.70	0.11	0.72	0.97	105	12.70	11.43	1.27	1.93	**1.46**	**0.11**	0.21	0.80
44137	108	6.74	6.12	**0.62**	1.47	1.34	0.20	**0.42**	0.96	108	12.48	12.34	**0.14**	2.61	2.61	0.21	**0.44**	0.66
44138	108	4.99	4.86	**0.13**	1.03	1.02	0.20	0.31	0.94	108	10.91	10.72	**0.19**	1.84	1.83	0.17	0.48	0.77
44139	108	5.37	6.60	−1.23	1.89	1.43	0.27	0.88	0.93	108	11.02	12.87	−1.85	3.64	3.14	0.28	0.66	0.63
44140	108	4.23	4.30	**−0.06**	**0.61**	0.60	0.14	**0.52**	0.95	108	11.77	10.59	1.18	2.14	1.79	0.15	0.25	**0.74**
44141	108	5.93	4.71	1.22	1.71	1.20	0.20	0.18	**0.98**	108	11.32	9.77	1.55	2.02	1.30	0.12	0.07	0.88
All	954	5.51	5.52	**−0.01**	1.22	1.22	0.22	**0.53**	0.91	954	12.13	11.62	**0.51**	2.29	2.23	0.18	**0.35**	0.70
Deep	746	5.45	5.35	0.10	1.29	1.29	0.24	**0.50**	0.90	746	12.11	11.81	**0.30**	2.37	2.35	0.19	**0.38**	0.70
OWI3G																		
41001	108	5.74	5.90	−0.16	**0.49**	**0.47**	**0.08**	0.34	**0.93**	108	13.25	13.01	0.24	2.06	2.05	0.15	0.53	0.78
41002	98	5.11	5.14	**−0.03**	**0.76**	**0.76**	**0.15**	**0.50**	**0.80**	98	14.23	13.09	1.14	1.60	1.13	0.08	0.84	0.93
44008	103	5.19	6.05	−0.86	1.29	0.96	0.19	0.13	**0.96**	103	11.65	11.85	**−0.20**	2.49	2.48	0.21	0.43	0.53
44011	105	6.25	6.36	−0.11	0.98	0.98	0.16	**0.53**	0.97	105	12.70	11.70	1.00	2.01	1.75	0.14	0.77	0.80
44137	108	6.74	5.82	0.92	**1.34**	**0.98**	**0.15**	0.86	0.98	108	12.48	11.10	1.38	1.82	1.19	0.10	0.89	0.94
44138	108	4.99	4.73	0.26	**0.84**	**0.80**	**0.16**	0.76	**0.98**	108	10.91	10.19	0.72	2.17	2.05	0.19	0.58	0.80
44139	108	5.37	5.34	**0.03**	0.80	0.80	0.15	0.75	**0.98**	108	11.02	9.54	1.48	2.26	1.71	0.15	0.86	0.90
44140	108	4.23	3.72	0.52	0.80	0.61	0.14	0.81	**0.97**	108	11.77	10.57	1.20	2.05	**1.66**	**0.14**	0.74	0.72
44141	108	5.93	4.68	1.26	1.57	**0.94**	**0.16**	0.94	**0.98**	108	11.32	9.63	1.69	2.29	1.54	0.14	0.94	0.93
All	954	5.51	5.30	0.21	**1.04**	**1.02**	**0.18**	0.63	**0.94**	954	12.13	11.16	0.97	2.10	1.87	0.15	0.73	**0.83**
Deep	746	5.45	5.04	0.41	**1.01**	**0.92**	**0.17**	0.29	**0.95**	746	12.11	10.99	1.12	2.05	1.72	0.14	0.23	**0.87**
WAM4																		
41001	108	5.74	5.93	−0.19	0.64	0.61	0.11	**0.38**	0.90	108	13.25	13.33	−0.08	2.32	2.32	0.17	0.53	0.73
41002	98	5.11	5.03	0.07	0.78	0.78	**0.15**	**0.50**	**0.80**	98	14.23	13.38	0.85	1.47	1.20	0.08	0.83	0.92
44008	103	5.19	6.08	−0.89	1.54	1.26	0.24	0.26	**0.96**	103	11.65	12.48	−0.83	2.80	2.67	0.23	0.43	0.59
44011	105	6.25	6.27	**−0.02**	1.30	1.29	0.21	0.67	0.97	105	12.70	12.21	**0.49**	**1.60**	1.53	0.12	**0.70**	**0.87**
44137	108	6.74	5.77	0.97	1.41	1.02	**0.15**	0.87	0.98	108	12.48	11.54	0.95	**1.31**	**0.90**	**0.07**	0.87	**0.96**
44138	108	4.99	4.66	0.33	0.98	0.93	0.19	0.74	0.97	108	10.91	10.46	0.45	2.15	2.10	0.19	**0.50**	0.69
44139	108	5.37	5.56	−0.19	1.28	1.26	0.24	**0.70**	0.97	108	11.02	9.91	1.12	2.01	1.67	0.15	0.81	**0.91**
44140	108	4.23	3.70	0.53	0.75	**0.53**	**0.13**	0.83	**0.97**	108	11.77	10.81	0.96	1.98	1.73	0.15	0.61	0.73
44141	108	5.93	4.56	1.37	1.74	1.06	0.18	0.94	0.97	108	11.32	9.96	1.36	1.88	**1.29**	**0.11**	0.90	0.95
All	954	5.51	5.28	0.23	1.21	1.19	0.22	0.66	0.93	954	12.13	11.54	0.59	1.99	1.90	0.16	0.69	0.82
Deep	746	5.45	5.03	0.42	1.15	1.07	0.20	0.29	0.94	746	12.11	11.31	0.80	1.91	1.73	0.14	0.28	0.86

SI—scatter index; *R*–ratio of points above and below 45° line; CC—correlation coefficient; Deep—statistics for all deep water buoys only.

bias (hindcast-measured)

$$b = \frac{1}{n} \sum_i (h_i - m_i); \qquad (9)$$

root-mean-square difference

$$\mathrm{rmsd} = \left[\frac{\sum_i (h_i - m_i)^2}{n} \right]^{0.5}; \qquad (10)$$

TABLE 4. Storm peak measured and hindcast wave height and period at buoys in the Halloween storm for four wave models.

	Measured			OWI1G			Resio2G			OWI3G			WAM4		
Buoy	HS	TP	DD/HH	HS	TP	DD/HH	HS	TP	DD/HH	HS	TP	DD/HH	HS	TP	DD/HH
41001	7.7	20.0	31/05	6.8	18.7	31/01	7.8	12.5	29/07	7.8	18.2	31/02	8.1	18.2	31/02
41002	7.8	20.0	31/10	6.2	13.7	30/18	5.9	14.3	29/19	6.6	16.3	30/21	6.7	16.9	30/22
44008	9.5	12.6	30/23	10.5	15.7	31/05	9.8	12.5	31/01	11.3	15.6	31/01	11.8	16.5	31/00
44011	11.8	17.8	30/16	12.0	16.1	30/18	12.9	14.3	30/19	12.8	16.1	30/16	13.7	16.9	30/15
44137	16.9	17.5	30/05	13.3	16.7	30/06	15.3	16.7	30/07	14.7	16.8	30/06	16.2	17.0	30/06
44138	11.5	13.7	29/16	11.3	14.2	29/20	11.2	14.3	30/00	11.7	14.4	29/20	12.7	14.4	29/20
44139	10.5	14.2	29/16	10.6	14.0	29/20	12.3	14.3	29/21	11.7	14.4	29/20	12.8	15.3	29/22
44140	8.1	12.2	29/23	8.8	13.2	30/02	8.6	14.3	30/01	7.0	12.5	30/02	7.5	12.9	30/01
44141	14.6	16.0	30/01	10.3	14.1	30/04	10.7	14.3	30/05	11.5	15.5	30/02	11.5	15.6	30/01

HS—significant wave height (m); TP—peak period (s); DD/HH—day/hour of maximum HS.
Measured wave height and peak period are smoothed using a 1,1,1 running average.

standard deviation of difference

$$\sigma_d = \left[\frac{\sum_i (h_i - m_i - b)^2}{n - 1}\right]^{0.5}; \tag{11}$$

scatter index

$$\mathrm{SI} = \frac{\sigma_d}{m}; \tag{12}$$

ratio (where $\delta = 1$ if $h_i \geqslant m_i$, $\delta = 0$ if $h_i < m_i$)

$$R = \frac{1}{n}\sum_1^n i\delta; \tag{13}$$

correlation coefficient

$$\mathrm{CC} = \frac{\sum_i [(h_i - \bar{h})(m_i - \bar{m})]/n}{[\sum_i (m_i - \bar{m})^2/n^{0.5}][\sum_i (h_i - \bar{h})2/n]^{0.5}}. \tag{14}$$

Time histories of HS and TP were also plotted at all buoys sites evaluated.

a. Halloween storm

A general impression of the behavior and performance of the alternative wave models is gained through Fig. 11, which gives scatterplots for each model between hindcast and measured time histories of HS for all nine buoys, and Table 3, which gives the comparative statistics of HS and TP at all buoys and aggregate statistics over all nine buoys combined and over only the seven buoys, which are moored in deep water (i.e., excluding 44008 and 44011). The first 72 h of the hindcast period, which was reserved for model spinup, are omitted from these comparisons.

We have indicated in boldface in Table 3 for each buoy/statistic the model with the most favorable behavior. First, it should be noted that all of these wave models provide extremely skillful hindcasts in the aggregate. For HS, the mean difference varies from between −0.01 m for Resio2G to 0.23 m for WAM4. Here SI varies from only 0.17 for OWI3G to 0.24 for Resio2G. The correlation coefficients vary over the narrow range 0.91–0.94. No model clearly outperforms any other in specification of time histories of HS in this storm. Differences between the models in specification of TP are slightly more apparent. Both 3G models show about a 1-s negative bias in TP, a common property of previous validations of WAM (e.g., Cardone et al. 1994), Resio2G is the least biased in TP albeit at the expense of its having the greatest scatter with SI of 0.19 relative to the OWI1G model, which exhibits the smallest SI in TP of 0.13.

TABLE 5. Statistics of differences between storm peak measured and hindcast wave height and period at buoys in the Halloween storm for four wave models.

	Significant wave height (m)								Peak period (s)							
Model	Avg meas	Avg hind	Mean diff	rms diff	Std dev	SI	*R*	CC	Avg meas	Avg hind	Mean diff	rms diff	Std dev	SI	*R*	CC
OWI1G	10.9	10.0	0.94	2.01	1.78	0.16	0.56	0.81	16.0	15.1	0.87	2.58	2.43	0.15	0.67	0.52
Resio2G	10.9	10.5	0.41	1.71	1.66	0.15	0.56	0.84	16.0	14.2	1.85	3.49	2.96	0.18	0.33	0.09
OWI3G	10.9	10.6	0.35	1.59	1.55	0.14	0.44	0.86	16.0	15.6	0.46	1.83	1.77	0.11	0.56	0.83
WAM4	10.9	11.2	−0.28	1.73	1.71	0.16	0.44	0.84	16.0	16.0	0.05	1.87	1.87	0.12	0.56	0.79

SI—scatter index; *R*—ratio of points above and below 45° line; CC—correlation coefficient.

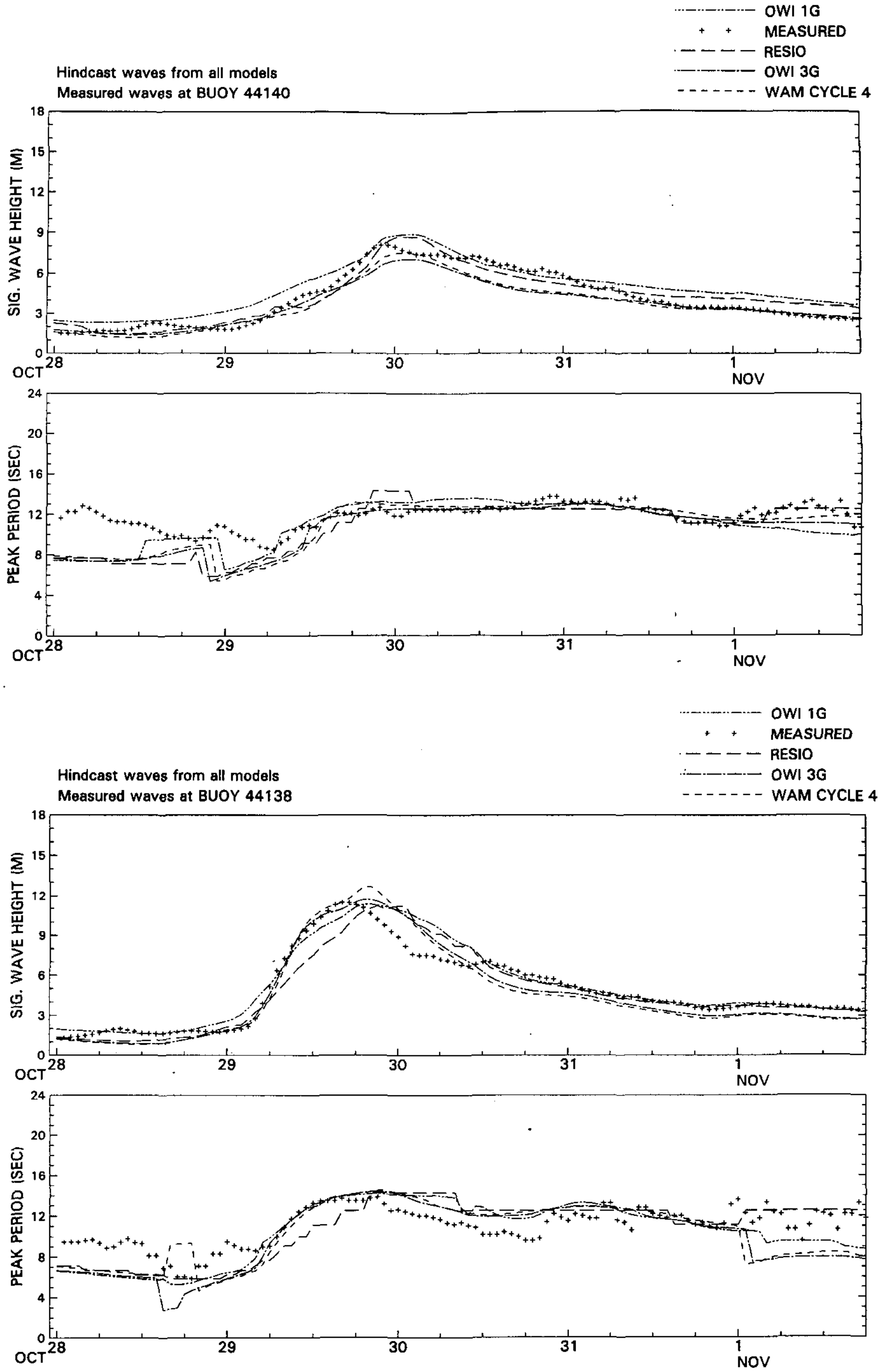

FIG. 12. Comparison of hindcast and measured time histories wave height and period in the Halloween storm at six selected buoys for four models.

The scatterplots show in addition that below HS of about 6 m there is relatively little difference between the model hindcasts of HS except for slight level shifts, which probably arise from small differences in model tuning. In the range of HS between 6 and 12 m the scatter increases for all models but the hindcasts are basically unbiased. Above 12 m, where most of the points are contributed by buoy 44137, there is some stratification in performance by model with WAM4 closest to the 45° line though still slightly negatively

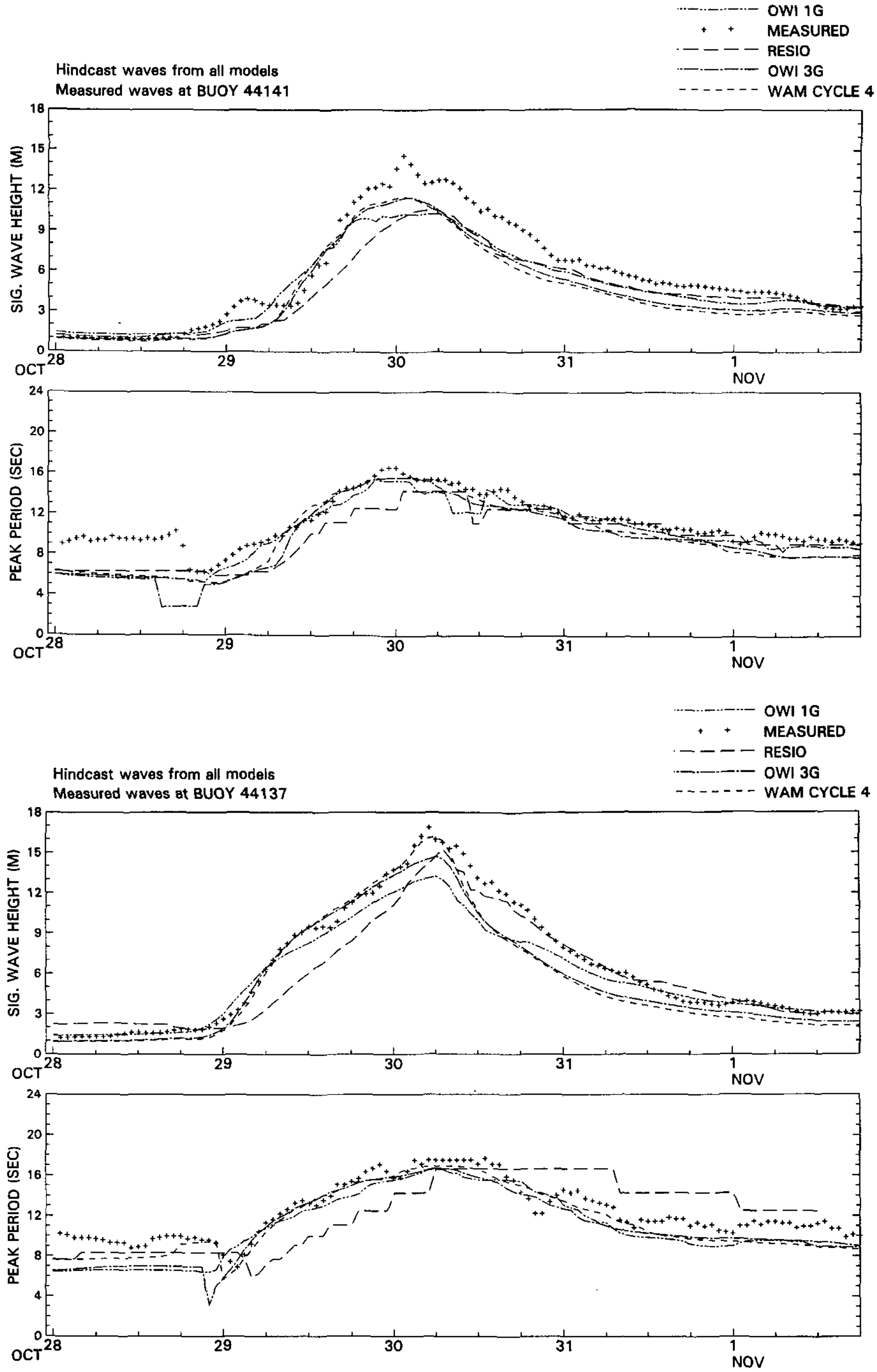

Fig. 12. (*Continued*)

biased at the highest sea states. OWI1G is the most negatively biased at ESSs, while OWI3G and Resio2G behave very much like WAM4.

Table 3 also shows that there are some variations in model skill rank from site to site that may be illustrated through comparisons of time histories of measured-hindcast time histories of HS and TP at individual buoys as follows (see Fig. 12). At 44140, which is at the extreme upwind end of the principal northeasterly fetch of the storm, there is about a 2-m spread in the time histories of HS (OWI1G highest, OWI3G lowest), with this envelope generally straddling the measured time history during the 48-h period centered on the peak. The measured and hindcast TP histories are

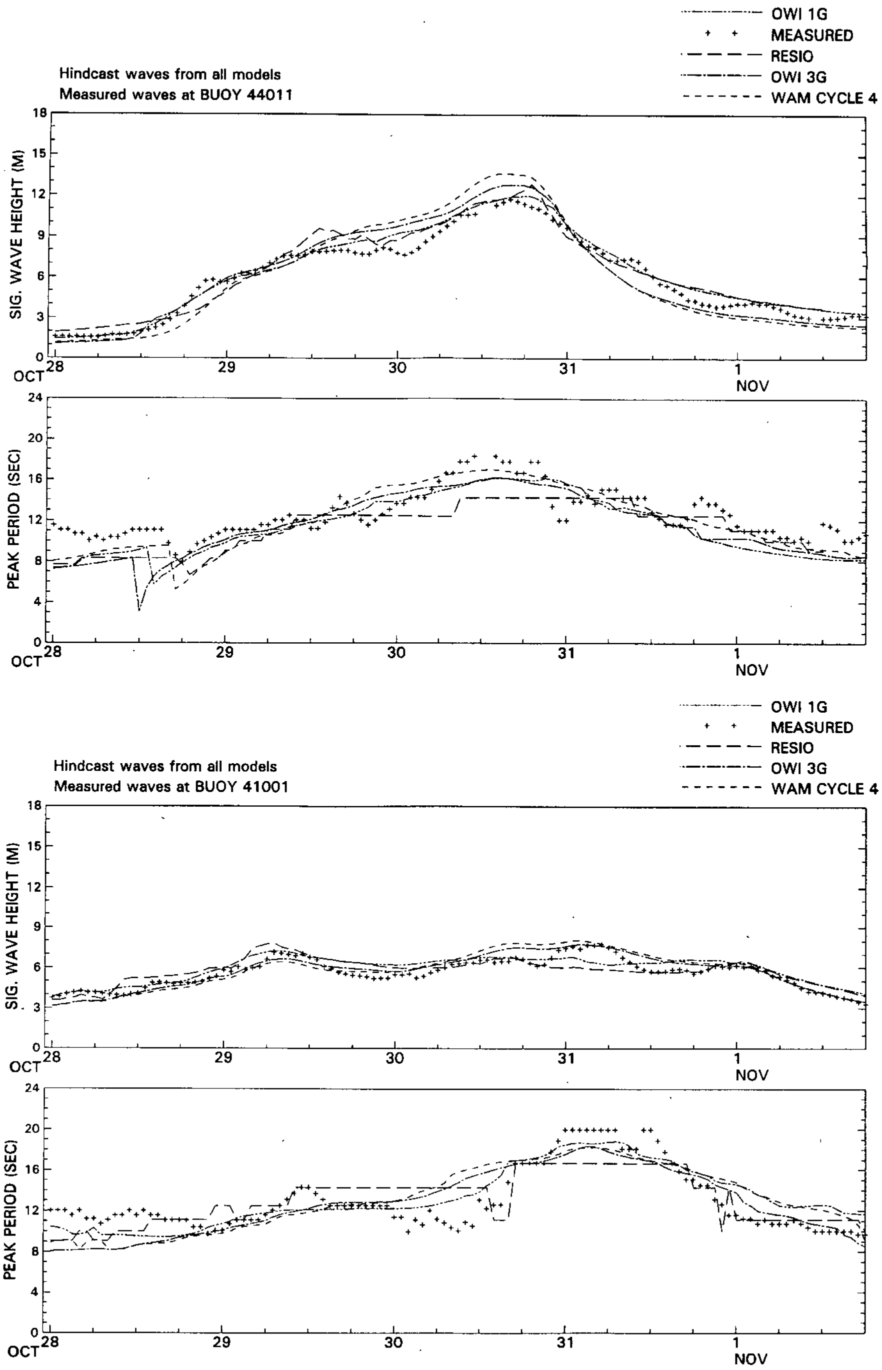

FIG. 12. (*Continued*)

all in close agreement during this period as well. At 44138, the models lag the growth stage and lead the decay stage in the local time history of HS by 3–6 h, with very good agreement between hindcast and modeled storm peak HS and associated TP for all models. At 44141, the southernmost of the buoys, all models underspecify the part of the storm during which HS exceeds about 8 m. In this regard, this time history stands out from all of the others. This buoy is in the vicinity of the north wall of the Gulf Stream during HOS and perhaps the deficiency in the hindcasts here arises in interaction of the growth with currents in the stream or a detached eddy. At 44137, one of two buoys that experienced ESS's in HOS, Resio2G lags in

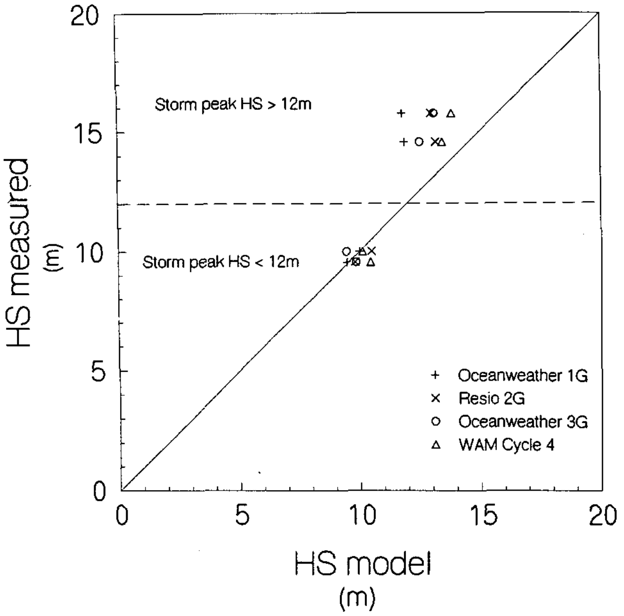

FIG. 13. Average of measured and model hindcast storm peak HS in HOS and SOC over groups of sites representing measured HS peaks above and below 12 m.

growth (as seen also at 44141) with respect to the other models but ultimately yields the second highest specified peak sea state and matches the decay stage more closely than the other models. WAM4 and OWI3G follow the observed history closely on the growth phase of the storm here and decay too rapidly on the decay phase. WAM4 grows to within 1 m of the observed maximum ESS peak by virtue of an extra spurt in growth during the 3 h before the peak, which the other models fail to simulate. This "extra" growth may be a result of the wind–wave coupling included in WAM4's atmospheric input source term S_{in}. Despite the magnitude of the peak HS at 44137 in HOS, the sea state is still underdeveloped for a wind speed of 32 m s^{-1}, implying an enhancement to the coupling even in extreme storm sea conditions. (Note that when we are describing these time histories we use the term "growth" in the sense of local change in HS and TP; such changes may arise in propagation and/or wave generation and dissipation.) Downstream of the area of maximum waves, at 44011 and 41001, propagated swell becomes an increasingly more important component of the total sea state, and all models seem to agree more closely with each other and with the measurements in both HS and TP. At 44011, the tendency for all models to slightly overspecify HS may be due to neglect of shallow-water processes. Despite these differences in detailed model behavior there appears to be no systematic effect attributable to the model class. Indeed, when the models depart from the measurements they all tend to depart in the same sense.

In model applications to assess extreme wave climate it is the specification of the peak sea state at a site in a storm that is critical. Table 4 compares hindcast and observed storm peak HS and associated TP at nine buoys, and in Table 5 these differences are summarized statistically. The average measured storm peak HS over this sample set is nearly 11 m. The scatter index for peak HS varies only over a very narrow range of 0.14 (OWI3G) to 0.16 (WAM4). Only WAM4 exhibits slight positive bias at 0.28 m, and OWI1G has the largest negative bias of 0.94 m. However, as noted above in the scatterplots, the models fare best in specification of peaks in the range of HS up to 12 m or so. Considering the extreme storm peaks only at the two Canadian buoys that observed ESS (44137, 44141), the models peak HS were biased low by an average of 3.9 m for OWI1G, 2.7 m for Resio2G, 2.6 m for OWI3G, and 2.0 m for WAM4. This behavior is also shown in Fig. 13 as a scatterplot of mean peak HS by model for each HS range.

b. *Storm of the century*

The comparative scatterplots for SOC, based upon time histories at eight buoys, are shown in Fig. 14. The patterns of the scatter for each model resemble those for HOS remarkably, even though the two storms are very different in movement and structure. Table 6 gives the comparative statistics based upon time histories, excluding a 48-h spinup period. As shown for the HOS comparisons all hindcasts are basically very skillful compared to real time analyses of storms provided by these same models. The scatter index for HS varies from 0.18 for OWI3G to 0.25 for Resio2G. Mean difference in HS is smallest for Resio2G (+0.04 m) and largest for OWI1G (−0.39 m). The scatter in TP is least for OWI1G and largest for Resio2G, a manifestation of the tendency of the Resio2G model to lag the measurements at some buoys in the rate of decrease of TP following the time of occurrence of the peak sea state.

Typical time histories of hindcast and measured HS and TP in the SOC at five buoys are shown in Fig. 15, in order from southwest to northeast. At 41006 and 41002, the relatively simple structure to the measured and hindcast time histories reflect the approach and passage of the main JS (SOC-JS1) described in the last section. All models track the observed rapid increase in HS and TP during the approach of this JS from the southwest, and as seen in HOS all models fail to grow all the way to the measured peak. As seen in HOS at 44137 also, Resio2G lags the peak by about 3 h with lag in HS also on the decay side with little change in TP. The record peak ESS (for a U.S. buoy) measured at 41002 is underspecified by all models by between 2 and 4 m, in the same order as seen at 44137 in HOS; that is, from highest to lowest: WAM4, Resio2G, OWI3G, OWI1G. Even though HOS and SOC were very different types of extratropical storms, 44137 in

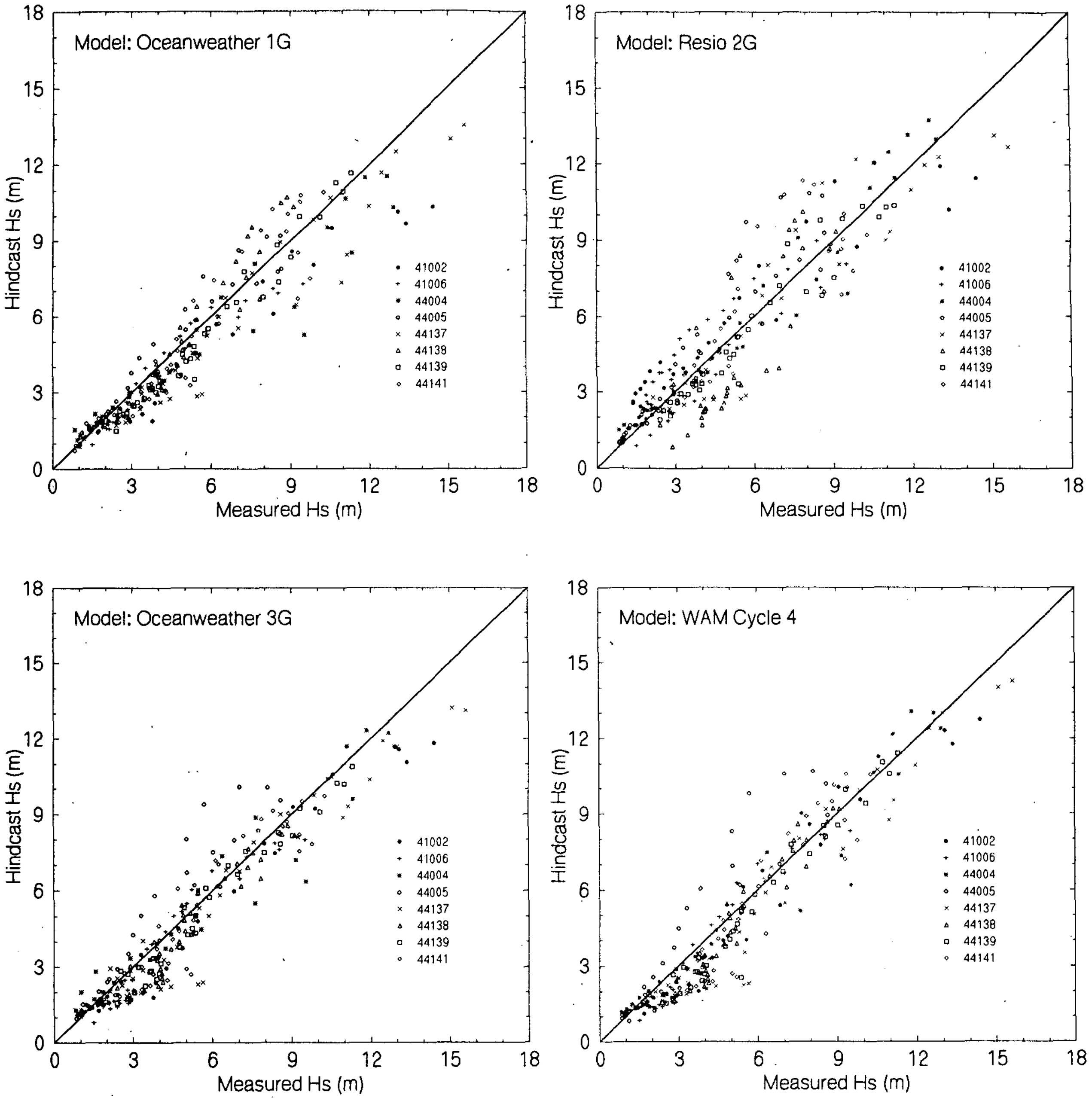

FIG. 14. Comparison of 3-h hindcast and measured wave at eight buoys in the storm of the century for four wave models.

HOS and 41002 in SOC both lay in the path of the core of propagating energetic JS's that could be tracked upstream over the previous 24 h at least, with core speeds of about 30 m s^{-1}.

At 44004, which lay outside the core of SOC-JS2, there is a double structure in the time histories reflecting first the influence of SOC-JS1 that approached from the south, followed by the influence of SOC-JS2 and its associated wave field, which approached from the southwest. All modeled time histories barely reflect the first maximum, associated with SOC-JS2, strongly suggesting that the common wind field is deficient in specifying the previous history and intensity of this feature. The main peak is generally well hindcast with the models exhibiting about a 2-m spread about the measured peak. Farther downstream at 44137, the dual-peak structure in the time histories is also evident. Again as at 44004, the first peak is barely indicated in the models. The main HS peak associated with SOC-JS1 is underpredicted by about 2–3 m by all models. However, TP is well specified during the

TABLE 6. Comparison statistics of 3-h measured and hindcast wave height and period at buoys in the storm of the century for four wave models.

Buoy	Significant wave height (m)									Peak period (s)								
	No. pts	Avg meas	Avg hind	Mean diff	rms diff	Std dev	SI	*R*	CC	No. pts	Avg meas	Avg hind	Mean diff	rms diff	Std dev	SI	*R*	CC
OWI1G																		
41002	33	4.91	4.04	−0.86	1.39	1.09	0.22	**0.27**	0.98	33	9.23	8.92	−0.31	1.01	0.96	0.10	0.39	**0.97**
41006	33	3.82	3.36	−0.45	0.73	**0.57**	**0.15**	0.18	**0.97**	33	8.71	8.38	−0.33	**0.64**	**0.55**	**0.06**	0.21	**0.96**
44004	33	5.03	4.48	−0.55	1.26	1.13	0.22	0.42	0.97	33	9.64	9.78	**0.14**	2.10	2.10	0.22	0.67	0.83
44005	33	4.01	4.26	**0.25**	**0.69**	**0.65**	**0.16**	**0.64**	**0.97**	33	8.19	10.54	2.35	3.61	2.73	0.33	0.88	0.73
44137	33	6.85	5.81	−1.04	1.45	1.01	0.15	0.15	**0.97**	33	11.76	11.51	−0.25	**1.38**	**1.36**	**0.12**	0.39	**0.92**
44138	33	5.42	5.52	**0.10**	0.93	0.93	0.17	**0.45**	**0.96**	33	12.35	12.35	**0.00**	**1.78**	**1.78**	**0.14**	**0.45**	**0.83**
44139	33	5.85	5.36	−0.49	**0.73**	0.54	**0.09**	0.15	**0.99**	33	13.05	12.21	−0.84	**1.62**	**1.39**	**0.11**	0.24	0.93
44141	33	5.87	5.77	**−0.09**	1.12	1.12	0.19	0.39	0.93	33	12.71	12.16	−0.55	**1.03**	**0.87**	**0.07**	0.30	**0.96**
All	264	5.22	4.83	−0.39	1.08	1.00	0.19	0.33	0.95	264	10.71	10.73	**0.02**	**1.86**	**1.86**	**0.17**	0.44	**0.86**
Resio2G																		
41002	33	4.91	5.37	**0.46**	1.33	1.24	0.25	0.76	0.95	33	9.23	11.89	2.65	3.99	2.98	0.32	0.82	0.56
41006	33	3.82	4.15	**0.33**	1.07	1.02	0.27	**0.61**	0.89	33	8.71	11.02	2.31	3.73	2.93	0.34	0.64	0.42
44004	33	5.03	5.14	**0.11**	**0.79**	**0.79**	**0.16**	0.67	**0.98**	33	9.64	9.80	0.17	**1.68**	**1.67**	**0.17**	**0.61**	**0.88**
44005	33	4.01	4.74	0.73	1.35	1.13	0.28	0.73	0.94	33	8.19	9.12	**0.93**	**1.67**	**1.39**	**0.17**	**0.73**	**0.87**
44137	33	6.85	6.50	**−0.35**	1.41	1.36	0.20	**0.33**	0.94	33	11.76	11.77	**0.01**	1.55	1.55	0.13	0.45	0.87
44138	33	5.42	4.60	−0.81	1.93	1.76	0.32	0.30	0.83	33	12.35	10.52	−1.83	3.70	3.21	0.26	0.33	0.50
44139	33	5.85	5.42	**0.44**	0.84	0.72	0.12	**0.18**	0.97	33	13.05	11.47	−1.58	2.38	1.78	0.14	0.15	0.85
44141	33	5.87	6.16	0.29	1.53	1.50	0.26	**0.42**	0.84	33	12.71	12.25	−0.46	1.27	1.18	0.09	0.36	0.91
All	264	5.22	5.26	**0.04**	1.33	1.33	0.25	**0.50**	0.91	264	10.71	10.98	0.28	2.71	2.70	0.25	**0.51**	0.68
OWI3G																		
41002	33	4.91	4.27	−0.63	0.95	0.71	0.15	0.12	0.98	33	9.23	8.86	−0.37	**0.89**	**0.81**	**0.09**	0.33	**0.97**
41006	33	3.82	3.41	−0.41	**0.72**	0.59	**0.15**	0.27	**0.97**	33	8.71	8.25	−0.46	0.88	0.75	0.09	0.30	0.95
44004	33	5.03	4.89	−0.14	0.97	0.96	0.19	0.61	0.97	33	9.64	10.01	0.37	1.90	1.86	0.19	0.64	0.86
44005	33	4.01	4.69	0.68	1.30	1.12	0.28	0.73	0.94	33	8.19	11.04	2.85	4.09	2.94	0.36	0.82	0.63
44137	33	6.85	5.97	−0.88	1.36	1.03	0.15	0.18	0.96	33	11.76	11.57	−0.19	1.49	1.48	0.13	**0.52**	0.90
44138	33	5.42	4.91	−0.50	**0.82**	**0.65**	**0.12**	0.27	0.95	33	12.35	12.30	−0.05	2.00	2.00	0.16	**0.55**	0.81
44139	33	5.85	5.31	−0.54	0.74	**0.50**	**0.09**	0.15	0.98	33	13.05	12.06	−0.99	2.01	1.75	0.13	0.30	0.89
44141	33	5.87	5.50	−0.37	**1.06**	**1.00**	**0.17**	0.36	0.93	33	12.71	12.31	−0.41	1.32	1.26	0.10	0.42	0.93
All	264	5.22	4.87	−0.35	**1.02**	**0.95**	**0.18**	0.34	**0.95**	264	10.71	1.080	0.09	2.06	2.06	0.19	0.48	0.83
WAM4																		
41002	33	4.91	4.42	−0.49	**0.81**	**0.65**	**0.13**	0.12	**0.99**	33	9.23	9.30	**0.06**	1.07	1.07	0.12	**0.45**	0.95
41006	33	3.82	3.41	−0.40	0.75	0.64	0.17	0.24	**0.97**	33	8.71	8.53	**−0.18**	0.70	0.67	0.08	**0.39**	**0.96**
44004	33	5.03	4.88	−0.15	0.97	0.96	0.19	**0.55**	0.97	33	9.64	10.55	0.91	2.35	2.17	0.23	0.64	0.82
44005	33	4.01	4.57	0.56	1.52	1.42	0.35	0.67	0.90	33	8.19	11.27	3.08	4.57	3.38	0.41	0.76	0.55
44137	33	6.85	5.90	−0.96	**1.35**	**0.95**	**0.14**	0.15	**0.97**	33	11.76	12.41	0.65	1.80	1.68	0.14	0.55	0.90
44138	33	5.42	4.95	−0.46	0.88	0.75	0.14	0.36	**0.96**	33	12.35	12.93	0.58	2.20	2.12	0.17	0.61	**0.83**
44139	33	5.85	5.24	−0.61	0.89	0.64	0.11	0.15	0.98	33	13.05	12.53	**−0.52**	1.75	1.67	0.13	**0.42**	**0.94**
44141	33	5.87	5.47	−0.40	1.16	1.09	0.19	0.39	**0.94**	33	12.71	12.83	**0.12**	1.29	1.29	0.10	**0.55**	**0.96**
All	264	5.22	4.86	−0.36	1.07	1.01	0.19	0.33	**0.95**	264	10.71	11.29	0.59	2.26	2.18	0.20	0.55	0.83

SI—scatter index; *R*—ratio of points above and below 45° line; CC—correlation coefficient.

growth and approach to the peak by all models. Downstream of 44137, at 44138, which lay well to the right of the core of SOC-JS1, the models are in much better agreement with the measurements.

Table 7 compares hindcast and observed peaks of HS and associated TP at eight buoys, and in Table 8 these differences are summarized statistically. The average measured storm peak HS over this sample set is 11.70 m, slightly greater even than for the HOS dataset. The scatter index for HS varies only over a very narrow range of 0.10 (OWI3G and WAM4 tie) to 0.15 (OWI1G). All models exhibit a negative bias in HS, which in both OWI models is about 1 m. Resio2G exhibits the smallest mean difference in peak HS and the lowest mean difference and scatter index in TP. However, as also seen in the HOS comparisons of peaks, the model biases in peak HS are negligible for HS less than 12 m and negative for HS greater than 12 m. Considering only the three buoys at which peak HS attained ESS levels (41002, 44004, 44137), the mean negative bias in modeled peak SWH was 2.7 m for OWI1G, 1.4 m for Resio2G, 2.0 m for OWI3G, and 1.1 m for

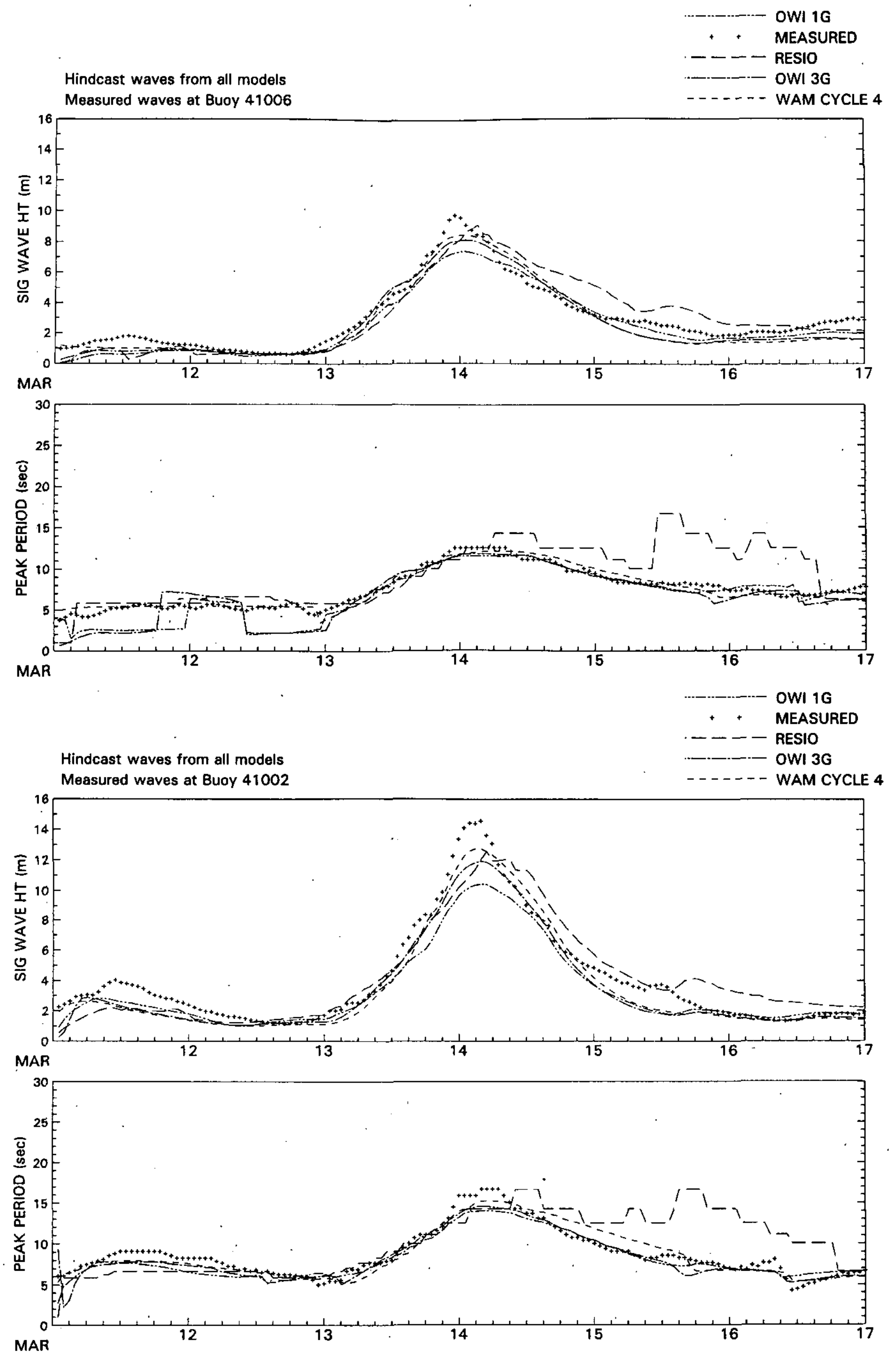

FIG. 15. Comparison of hindcast and measured time histories wave height and period in the storm of the century at five selected buoys for four models.

WAM4. The pattern of bias for each regime, shown in Fig. 13, is remarkably like that found in HOS.

6. Summary and conclusions

In this study, four widely applied spectral wave models, namely, the Oceanweather 1G and 3G models, a 2G wave model, and the latest cycle (WAM4) of the WAM 3G model are adapted to the western North Atlantic basin on grid systems with common resolution, and are driven by common wind fields for both storms. The wind fields were developed using careful manual kinematic reanalysis using all conventional data, including ship and buoy observations received too late

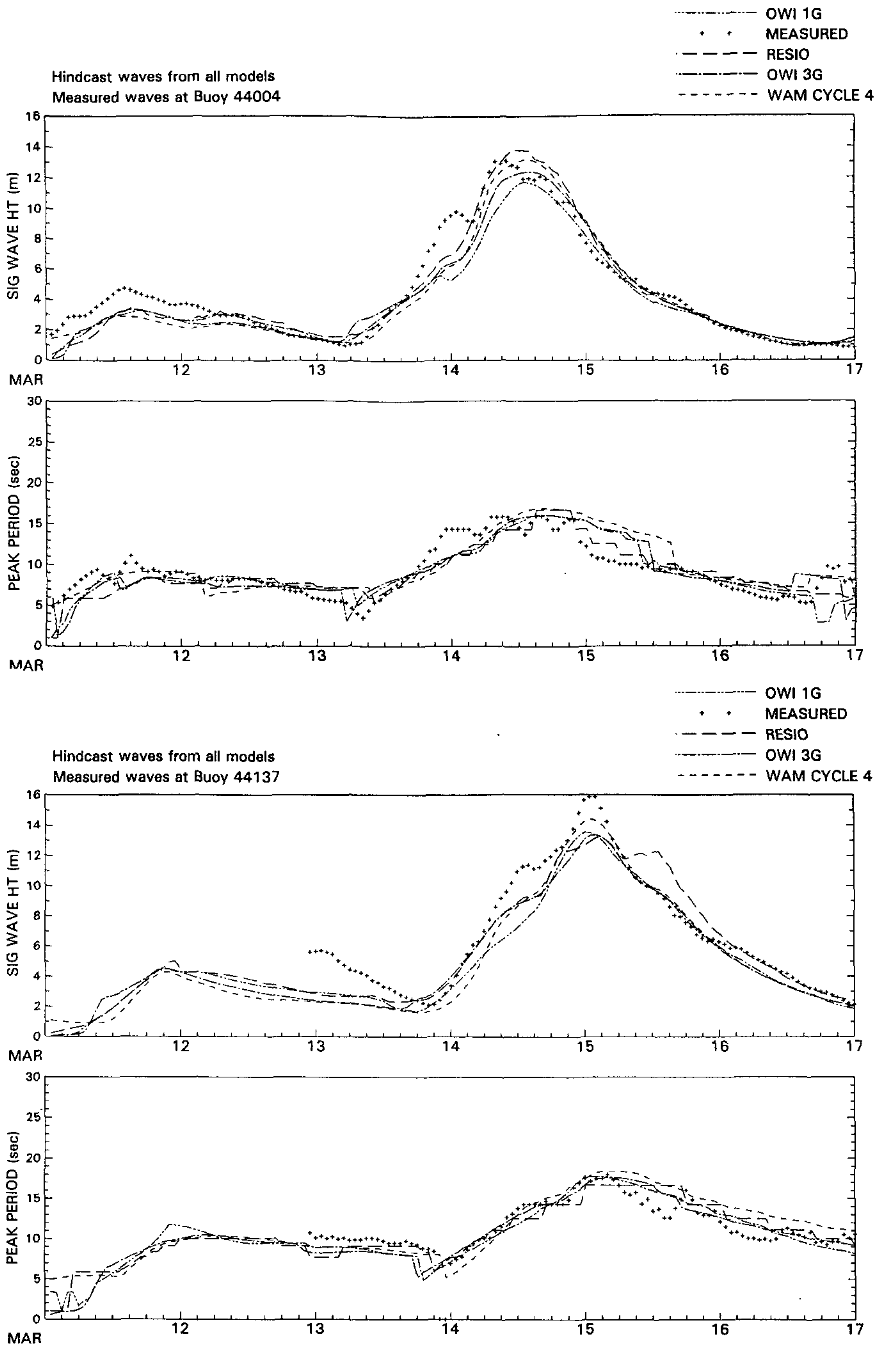

FIG. 15. (*Continued*)

for use in real time. A crucial part of this analysis is the adjustment of buoy wind speeds to the 20-m effective neutral surface wind for anemometer height, stability, and averaging interval effects. A sea-state-dependent bias between vector- and scalar-averaged derived measured wind speeds was inferred from the measurements and was used to increase vector-averaged buoy wind speeds by up to 12% in the most extreme sea states.

Wave hindcasts were evaluated against time series of measured HS, dominant wave period and wave spectra obtained at nine U.S. and Canadian buoys moored in deep water between offshore Georgia and Newfoundland. We conclude from our analyses that

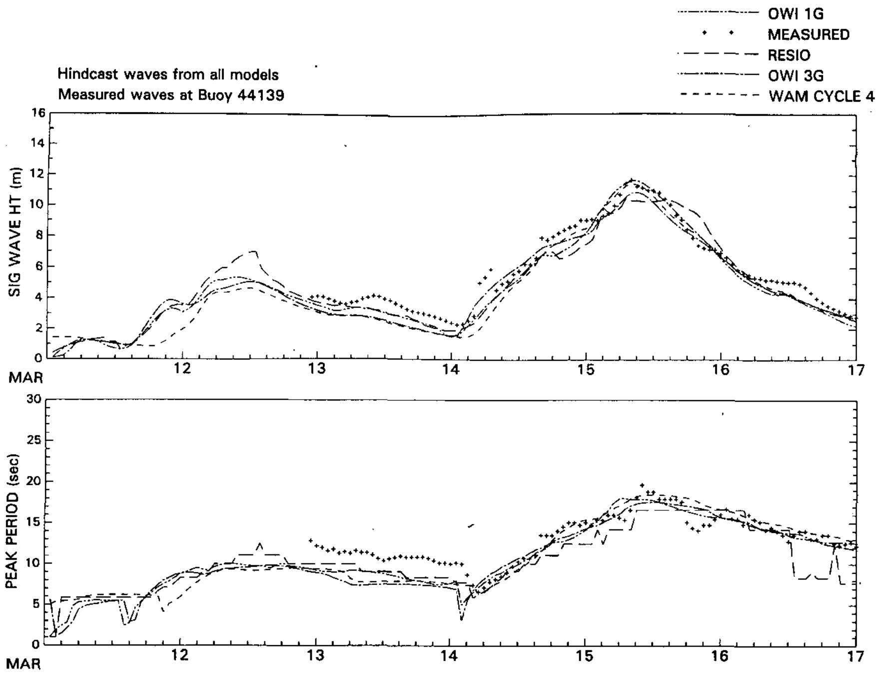

FIG. 15. (*Continued*)

all wave models investigated here performed very well for wave conditions up to about 12 m HS. These hindcasts exhibit considerably greater skill than real-time wave analyses derived by some of these same models operating at U.S., Canadian and European centers, confirming that the typically large errors in operational surface marine wind field analyses are the dominant source of errors in operational wave analyses and forecasts.

In contrast with the successful performance of the wave models in sea states up to 12 m, all models tended to underpredict the most extreme sea states. It is unclear whether this disagreement is due to remaining uncertainties in the wind field or to biases in the wave models at high sea states. Despite the large differences in the parameterization of the physics between the models, differences in skill in specifications of time histories of HS, TP, and spectral shape (spectral comparisons were made but are not shown) averaged over all buoys were relatively slight. It was noted that when the models disagree with the measurements in time series comparisons, they tended to disagree in the same sense, suggesting a source either in residual wind field errors or remaining deficiencies in wave model physics common to all classes of models.

A common phenomenological link between the extremely high waves in these storms appears to be wave generation along a dynamic fetch associated with in-

TABLE 7. Storm peak measured and hindcast wave height and period at buoys in the storm of the century for four wave models.

	Measured			OWI1G			Resio2G			OWI3G			WAM4		
Buoy	HS	TP	DD/HH	HS	TP	DD/HH	HS	TP	DD/HH	HS	TP	DD/HH	HS	TP	DD/HH
41002	14.6	16.7	14/04	10.4	14.0	14/04	12.5	14.3	14/05	11.9	14.6	14/04	12.7	15.0	14/03
41006	9.7	12.5	13/23	7.2	11.5	14/00	9.0	12.5	14/03	8.0	11.8	14/01	8.4	11.8	14/01
44004	13.1	15.3	14/10	11.7	15.5	14/13	13.8	14.3	14/11	12.3	15.9	14/14	13.2	16.7	14/14
44005	8.9	12.6	14/13	9.3	15.6	14/19	11.3	14.3	14/22	10.1	16.3	14/22	10.7	16.7	14/22
44014	6.7	13.7	13/19	8.5	14.3	14/07				9.2	14.5	14/06	9.5	15.3	14/07
44137	15.9	17.5	15/02	13.5	17.6	15/00	13.2	16.7	15/02	13.4	17.4	15/02	14.4	18.0	15/01
44138	9.4	17.5	15/14	10.8	17.6	15/16	10.1	16.7	15/07	8.5	17.8	15/15	9.3	18.5	15/14
44139	11.7	16.6	15/08	11.7	18.0	15/08	10.6	14.3	15/07	10.9	17.4	15/09	11.5	18.1	15/08
44141	10.3	18.4	15/09	10.9	17.7	15/10	11.4	16.7	15/07	9.7	17.5	15/09	10.6	18.2	15/07

HS—significant wave height (m); TP—peak period (s); DD/HH—day/hour of maximum HS.
Measured wave height and peak period are smoothed using a 1,1,1 running average.

TABLE 8. Statistics of differences between storm peak measured and hindcast wave height and period at buoys in the storm of the century for four wave models.

	Significant wave height (m)								Peak period (s)							
Model	Avg meas	Avg hind	Mean diff	rms diff	Std dev	SI	R	CC	Avg meas	Avg hind	Mean diff	rms diff	Std dev	SI	R	CC
OWI1G	11.7	10.7	−1.01	2.06	1.80	0.15	0.38	0.67	15.9	15.9	0.05	1.57	1.57	0.10	0.63	0.73
Resio2G	11.7	11.5	−0.21	1.63	1.62	0.14	0.50	0.76	15.9	15.0	−0.91	1.25	1.25	0.08	0.13	0.81
OWI3G	11.7	10.6	−1.10	1.59	1.15	0.10	0.13	0.90	15.9	16.1	0.20	1.60	1.59	0.10	0.50	0.69
WAM4	11.7	11.4	−0.35	1.17	1.12	0.10	0.38	0.90	15.9	16.6	0.74	1.79	1.63	0.10	0.63	0.70

SI—scatter index; R—ratio of points above and below 45° line; CC—correlation coefficient.

tense surface wind maxima or jet streaks, which maintain high spatial coherency over at least 24 h and propagate at about speeds of 15–20 m s^{-1}. The ESSs are observed in these two storms only at those buoys directly in the path of the jet core of these features. Unfortunately, such detailed surface wind field features are resolvable only through kinematic analysis and only when these features evolve within the relatively dense network of buoys just off the east coast. This suggests that operational objective analyses and forecasts will have even greater negative biases in extreme storms. Consequently, such information should not be used for applications that require accurate specification of extreme sea states.

These results suggest strongly that for applications where supercomputers are not available, and especially for most operational applications where only integrated properties of the spectrum (e.g., HS, TP) are required or where errors in forcing wind fields are typical of real-time objective analyses and forecasts, highly developed and validated 1G and 2G wave models may continue to be used. However, accurate specification of ESS is especially critical for application of wave models to determine the extreme wave climate for ship, offshore, and coastal structure design. Therefore, further study is required to isolate the contribution of remaining wind field errors and model physics and numerics to the underprediction of ESS in these storms.

Finally, this study raises the possibility that very extreme sea states may be much more common than earlier thought in the waters off the East Coast of North America and suggests that the extreme wave climate needs to be updated, if not reevaluated altogether.

Acknowledgments. Support for this project was provided by the Canadian Federal Panel on Energy Research and Development. The manual analyses were performed at Oceanweather by a team of Meteorologists including B. T. Callahan, S. T. Keeney, and M. J. Parsons. The work conducted by R. E. Jensen was performed under the Coastal Flooding and Storm Protection Program of the U.S. Army Engineers General Investigation Research and Development Program; permission to publish is granted by the Chief of Engineers.

REFERENCES

Axys Environmental Systems, 1992: Operations/maintenance/reference manual for NOMAD ZENO payloads. AXYS Environmental Systems, Sidney, BC, 60 pp. plus appendices.

Beal, R. C., 1991: LEWEX: Motivation, objectives and results. *Directional Ocean Wave Spectra,* R. C. Beal, Ed., Johns Hopkins University Press, 2–12.

Burgers, G., 1990: A guide to the Nedwam wave model. Scientific Reports WR-90-04, Koninklijk Nederlands Meteorologisch Instituut, 81 pp. [Available from KNMI, P.O. Box 201, 3730 AE de Bilt, Wilhelminalaan 10, Netherlands.]

Cameron, D., and G. Parkes, 1992: A meteorological overview of the Halloween Storm of 1991. Preprints, *Third Int. Workshop on Wave Hindcasting and Forecasting,* Montreal, PQ, Canada, Atmospheric Environment Service, S1–S44.

Cardone, V. J., 1969: Specification of the wind distribution in the marine boundary layer for wave forecasting, 131 pp. [NTIS AD 702 490.]

——, 1991: The LEWEX wind fields and baseline hindcast. *Directional Ocean Wave Spectra,* R. C. Beal, Ed., The Johns Hopkins University Press, 136–146.

——, 1992: On the structure of the marine wind field in extratropical storms. Preprints, *Third Int. Workshop on Wave Hindcasting and Forecasting,* Montreal, PQ, Canada, Atmospheric Environment Service, 54–66.

——, and K. C. Ewans, 1992: Validation of the hindcast approach to the specification of wave conditions at the Maui location off the west coast of New Zealand. Preprints, *Third Int. Workshop on Wave Hindcasting and Forecasting,* Montreal, PQ, Canada, Atmospheric Environment Service, 232–247.

——, W. J. Pierson, and E. G. Ward, 1976: Hindcasting the directional spectra of hurricane generated waves. *J. Pet. Technol.,* **28,** 385–394.

——, A. J. Broccoli, C. V. Greenwood, and J. A. Greenwood, 1980: Error characteristics of extratropical storm wind fields specified from historical data. *J. Pet. Technol.,* **32,** 873–880.

——, J. G. Greenwood, and M. A. Cane, 1990: On trends in historical marine wind data. *J. Climate,* **3,** 113–127.

——, H. C. Graber, R. E. Jensen, S. Hasselmann, and M. J. Caruso, 1994: In search of the true surface wind field during SWADE IOP-1: Ocean wave modelling perspective. *The Global Atmosphere and Ocean System,* accepted.

Clancy, R. M., and W. D. Sadler, 1992: The Fleet Numerical Oceanography Center Suite of Oceanographic Models and Products. *Wea. Forecasting,* **7,** 307–327.

Corson, W. D., D. T. Resio, R. M. Brooks, B. A. Ebersole, R. E. Jensen, D. S. Ragsdale, and B. A. Tracy, 1981: Atlantic coast hindcast deepwater significant wave information. WIS Report

2, U.S. Army Engineer Waterways Experiment Station, Vicksburg, MS, 1272 pp.

Donelan, M., and W. J. Pierson, 1983: The sampling variability of estimates of spectra of wind-generated gravity waves. *J. Geophys. Res.,* **88**(C7), 4381–4392.

Eid, B. M., C. Morton, E. Dunlop, and T. Pierce, 1992: Development of wind and wave climate atlas for the east coast of Canada and the Great Lakes. Preprints, *Third Int. Workshop on Wave Hindcasting and Forecasting,* Montreal, PQ, Canada, Atmospheric Environment Service, 362–372.

Gilhousen, D. B., 1987: A field evaluation of NDBC moored buoy winds. *J. Atmos. Oceanic Technol.,* **4,** 94–104.

Greenwood, J. A., V. J. Cardone, and L. M. Lawson, 1985: Intercomparison test version of the SAIL wave model. *Ocean Wave Modelling, the SWAMP Group,* Plenum Press, 221–233.

Guillaume, A., 1990: Statistical tests for the comparison of surface gravity wave spectra with application to model validation. *J. Atmos. Oceanic Technol.,* **7,** 551–567.

Gunther, H., S. Hasselmann, and P. A. E. M. Janssen, 1991: Wamodel cycle 4. Tech. Rep. 4, Deutsches Klima Rechen Zentrum, edited by Modellberatungsgruppe, Hamburg, Germany, 91 pp.

Hasselmann, K., 1974: On the spectral dissipation of ocean waves due to whitecapping. *Bound.-Layer Meteor.,* **6,** 106–127.

Hasselmann, S., K. Hasselmann, J. H. Allender, and T. P. Barnett, 1985: Computations and parameterizations of the nonlinear energy transfer in a gravity-wave spectrum. Part II: Parameterization of the non-linear transfer for application in wave models. *J. Phys. Oceanogr.,* **15,** 1378–1391.

Janssen, P. A. E. M., 1991: Quasi-linear theory of wind wave generation applied to wave forecasting. *J. Phys. Oceanogr.,* **21,** 745–754.

Kahma, K. K., and C. J. Calkoen, 1992: Reconciling discrepancies in the observed growth of wind-generated waves. *J. Phys. Oceanogr.,* **22,** 1389–1404.

Khandekar, M. L., R. Lalbeharry, and V. J. Cardone, 1994: The performance of the Canadian spectral ocean wave model (CSOWM) during the Grand Banks ERS-1 SAR wave spectra validation experiment. *Atmos.–Ocean,* **32,** 31–60.

Kocin, P. J., D. A. Olson, A. F. Wick, and R. D. Harner, 1991: Surface weather analysis at the National Meteorological Center: Current problems and future plans. *Wea. Forecasting,* **6,** 289–298.

Komen, G. J., S. Hasselmann, and K. Hasselmann, 1984: On the existence of a fully developed windsea spectrum. *J. Phys. Oceanogr.,* **14,** 1271–1285.

Maat, N. C., C. Kraan, and W. A. Oost, 1991: The roughness of the wind waves. *Bound.-Layer Meteor.,* **54,** 89–103.

Nickerson, J. W., 1993: Freak waves! *Mar. Wea. Log,* **37,** 14–19.

NCDC, 1993a: NOAA Marine Environmental Data on CD-ROM. 14-disc set available from National Climatic Data Center, Asheville, NC.

——, 1993b: The Big One! National Climatic Data Center, Asheville, NC, 25 pp.

NOAA, 1992: The Halloween Nor'easter of 1991. Natural Disaster Survey Report. Available from U.S. Department of Commerce. 61 pp. plus Appendices.

Overland, J. E., and W. H. Gemmill, 1978: Marine winds in the New York Bight. *Mon. Wea. Rev.,* **105,** 1003–1008.

Reece, A. M., and V. J. Cardone, 1982: Test of wave hindcast model results against measurements during four meteorological systems. *Offshore Technology Conf.,* Houston, TX, 269–282.

Resio, D. T., 1981: The estimation of a wind wave spectrum in a discrete spectral model. *J. Phys. Oceanogr.,* **11,** 510–525.

——, and W. Perrie, 1989: Implications of an f^4 equilibrium range for wind-generated waves. *J. Phys. Oceanogr.,* **19,** 193–204.

Ross, D. B., V. J. Cardone, J. E. Overland, R. McPherson, W. J. Pierson, and S. W. Yu, 1980: Oceanic surface winds. *Advances in Geophysics,* Vol. 27, Academic Press, 101–139.

Sanders, F., 1990: Surface weather analysis over the oceans—Searching for sea truth. *Wea. Forecasting,* **5,** 596–612.

Snyder, R., F. W. Dobson, J. A. Elliott, and R. B. Long, 1981: Array measurements of atmospheric pressure fluctuations above surface gravity waves. *J. Fluid Mech.,* **102,** 1–59.

Swail, V. R., V. J. Cardone, and B. M. Eid, 1992: An extreme wind and wave hindcast off the west coast of Canada. Preprints, *Third Int. Workshop on Wave Hindcasting and Forecasting,* Montreal, PQ, Canada, Atmospheric Environment Service, 362–372.

Uccellini, L. W., S. F. Corfidi, N. W. Junker, P. J. Kocin, and D. A. Olson, 1992: Report on the Surface Analysis Workshop held at the National Meteorological Center, 25–28 March, 1991. *Bull. Amer. Meteor. Soc.,* **73,** 459–472.

Wu, J., 1982: Wind-stress coefficients over the sea surface from breeze to hurricane. *J. Geophys. Res.,* **87,** 9704–9706.